Applied Geochemistry 131 (2021) 105047

Contents lists available at ScienceDirect

Applied Geochemistry

journal homepage: www.elsevier.com/locate/apgeochem

Long-term retention and chemical fractionation of fissionogenic Cs and Tc in Oklo natural nuclear reactor fuel

Evan E. Groopman [a,*], Larry R. Nittler [b], David G. Willingham [a], Alex P. Meshik [c], Olga V. Pravdivtseva [c]

[a] *Material Science and Technology Division, U.S. Naval Research Laboratory, 4555 Overlook Avenue SW, Washington, DC, 20375, USA*
[b] *Department of Terrestrial Magnetism, Carnegie Institution of Science, 5241 Broad Branch Road, Washington, DC, 20015, USA*
[c] *Department of Physics, Washington University in St. Louis, One Brookings Drive, St. Louis, MO, 63130, USA*

ARTICLE INFO

Editorial handling by Dr GARETH LAW

Keywords:
Oklo
Natural nuclear reactor
Fission product
Cesium
Technetium
Fractionation
SIMS
AMS

ABSTRACT

We present the results of a coordinated NAUTILUS and NanoSIMS isotopic study of epsilon (ε) phase metallic aggregates from the Oklo natural nuclear reactor zone (RZ) 13. We observed that fissionogenic Tc and Cs were heterogeneously sequestered within the aggregates. Isotopes of these elements are relevant for improving the safety of spent nuclear fuel storage and reactor operation on generational timescales. Like the noble metals, nearly all of the Tc was retained within the reactor, though its abundance relative to Ru in the metallic aggregates varied by a factor of 10. The neutron fluence estimated from the production of ^{100}Ru from neutron capture on ^{99}Tc was estimated to be up to 1.2×10^{21} n·cm^{-2}. In contrast to Tc, nearly all of the fissionogenic Cs in the reactors was lost from the reactor fuel. The metallic aggregates contain the only phases yet identified to have sequestered radiocesium. Fissionogenic Cs isotopes decay over vastly different timescales, but were incorporated and retained within the ε-phase in proportions similar to stable ^{133}Cs. This indicates that retention began during criticality and sequestration lasted billions of years, despite local geologic activity and the presence of nearby magmatic dikes. Using fissionogenic Ba isotopes, we estimated that the metallic aggregates continually incorporated their radioactive Cs parents during criticality, though the majority of Cs was flushed out of the reactor on a characteristic timescale of 2.7 ± 0.6 years. We found that the abundance of Bi was correlated to Rh and Pd, and speculate that this may have been due to primary Np–Rh and Np–Pd alloys forming during or shortly after criticality. Using Pb–Pb data from uraninite and galena grains surrounding the metallic aggregates, we also inferred a final Pb mobility age of 298 Ma for RZ13, which is more recent than most estimates from other RZs.

1. Introduction

Understanding how fission products are retained or mobilized from nuclear fuel and in the environment is highly important for waste storage, safety, and diagnostic applications. The Oklo phenomenon (e.g., Bodu et al., 1972; De Laeter and Hidaka, 2007; Gauthier-Lafaye et al., 1996; Hidaka and Holliger, 1998; Ruffenach et al., 1976, and references therein) provides unique natural analogs for long-term nuclear waste storage. Two billion years ago, more than one dozen sites in Gabon experienced varied periods of underground criticality, resulting in the production, sequestration, and migration of abundant fission and burnup products. These sites illustrate the importance of local geological conditions with respect to the sequestration or loss of specific fissionogenic isotopes, and more generally, the complex chemical behavior of highly radioactive spent nuclear fuel (SNF). Elements were partitioned into primary and secondary mineral phases within the reactor fuel, during and since the end of criticality. Each of these phases preferentially sequestered specific fissionogenic signatures. Among the extensive array of radioactive fission products, the chemical behaviors of Cs and Tc were investigated here because of their large relative activities on the timescales of human generations and medium-term storage. Cesium, in particular, is volatile and water soluble, and has multiple relevant radioisotopes: ^{134}Cs ($t_{1/2} = 2.1$ y), ^{135}Cs ($t_{1/2} = 2.3$ Ma), ^{137}Cs ($t_{1/2} = 30$ y), which decay to stable Ba (Fig. A1). Recently it was discovered that fissionogenic Cs and Ba at Oklo were collocated with the secondary ε-phase metallic aggregates in Oklo RZ13 (Groopman et al., 2018). Previous bulk isotopic work found that the majority of fissionogenic Cs and Ba were lost from the reactor fuel, in large part due to the high

---

[*] Corresponding author.
E-mail addresses: evan.groopman@nrl.navy.mil, eegroopm@gmail.com (E.E. Groopman).

https://doi.org/10.1016/j.apgeochem.2021.105047
Received 8 March 2021; Received in revised form 12 May 2021; Accepted 25 June 2021

solubility and reactivity of Cs and its incompatibility with the UO_2 matrix (Brookins et al., 1975; Hidaka and Gauthier-Lafaye, 2008; Hidaka et al., 1992, 1993a). Hidaka (2020) provides a recent review of in situ isotopic studies targeting specific minerals phases within the reactor zones.

Oklo RZ13 experienced the shortest duration and highest flux of the natural reactors, lasting 24 ka with a neutron fluence of up to 7.8×10^{20}–1.1×10^{21} $n \cdot cm^{-2}$ (Hidaka and Holliger, 1998; Holliger, 1991; Meshik et al., 2000). The average power was roughly 100 kW, comparable to a small research reactor (Meshik et al., 2004). The neutron flux was roughly 5–30× higher than other RZs. In comparison, the RZ10 and Bangombé reactors experienced neutron fluences of 5.2×10^{20}–8.0×10^{20} $n \cdot cm^{-2}$ and 3.1×10^{20} $n \cdot cm^{-2}$, respectively, but with durations >5× longer than RZ13 (Hidaka and Holliger, 1998). RZ9 generated a neutron fluence of 3.6×10^{20} $n \cdot cm^{-2}$ over 220 ka, 10× longer than RZ13. RZ2 generated a fluence of 1.25×10^{21} $n \cdot cm^{-2}$ over a duration of 800 ka (Ruffenach et al., 1976). Hidaka and Holliger (1998) calculated that in RZ13 the relative fission contributions of ^{235}U, ^{238}U, and ^{239}Pu were 74.9%, 17.9%, and 7.2%, respectively. These represent the largest proportions of fission due to ^{239}Pu and ^{238}U of the Oklo RZs. Other zones typically had fission contributions closer to 90% ^{235}U, though these vary by several percent (Hidaka and Holliger, 1998; Loss et al., 1988). Neutrons in RZ13 were not well thermalized, characterized by a spectrum index, r (ratio of fast/thermal neutrons), of 0.241. In addition to the primary uraninite fuel, a variety of secondary mineral phases are present within the RZ13 core, including La–Ce–Sr–Ca aluminous hydroxy phosphate; sulfides, such as galena (PbS); calcite ($CaCO_3$); and metallic aggregates of Pb–Ru–Rh–Te–As–S and galena (Dymkov et al., 1997; Gauthier-Lafaye et al., 1996; Holliger, 1994). The metallic aggregates are of particular interest, as they consist predominantly of fissionogenic and radiogenic Ru, Rh, and Pb; they have been found to contain a range of ^{99}Ru enrichments and depletions relative to the expected fission yield, indicative of chemical partitioning of ^{99}Tc ($t_{1/2} = 0.21$ Ma) (Hidaka et al., 1993b, 1999). Radiolysis of water during criticality has been suggested as the mechanism by which changes in local redox conditions caused chemical fractionation via leaching between Tc and Ru in the aggregates and uraninite (Kikuchi et al., 2010; Savary and Pagel, 1997). The correlated presence of ^{100}Ru with present-day ^{99}Ru further indicates that the fractionation between Tc and Ru occurred during reactor criticality. Ruthenium-100 is shielded from β^- decay by ^{100}Mo ($t_{1/2} = 8.5 \times 10^{18}$ y), so it must have been produced by the *n*-capture reactions $^{99}\mathrm{Ru}\,(n,\gamma)^{100}\mathrm{Ru}$ and $^{99}\mathrm{Tc}\,(n,\gamma\beta^-)^{100}\mathrm{Ru}$ during criticality.

In anthropogenic reactors, the ε-phase typically consists of nanophase Mo–Ru–Pd-Tc-Rh particles and aggregates. Isotopes of Mo, Ru, Tc, Rh, and Pd constitute approximately 47% of the total thermal fission yield from ^{235}U (25% Mo, 6.1% Tc, 11.3% Ru, 3% Rh, 1.4% Pd). ε-phase metallic aggregates are present in the spent Oklo reactor fuel ranging in size from sub-μm to 150 μm in RZs 10 and 13 (e.g., Gauthier-Lafaye et al., 1996; Kikuchi et al., 2010). The Oklo metallic aggregates have been found to primarily consist of Pb–Ru–As–S and Pb–Te phases surrounded by galena and silicates of U and Zr (Gauthier-Lafaye et al., 1996). Typical aggregate compositions are shown in Table 1. Within the uraninite matrix, accumulations of Mo and Bi were found in RZ13, but were absent in RZ10. Notably, Mo concentrations in the Oklo aggregates were consistently below the detection limits of electron probe microanalysis (EPMA) for quantification (0.01 wt%), indicating that Mo had been fractionated strongly relative to the Pt-group elements. Using the sensitive high-resolution ion microprobe (SHRIMP), Kikuchi et al. (2010) detected the presence of Mo and Zr in the aggregates, however they did not report inter-element ion ratios. Utsunomiya and Ewing (2006) provided a timeline for the apparent alteration, with the original ε-phase being processed into ruthenarsenites (RuAs) and ruasite (RuAsS) by As-rich fluids, followed by release of all Mo and some Tc, and precipitation of galena. Dissolution experiments of metallic precipitates from SNF have shown that the leach rate of Mo > Tc > Ru ~ Rh ~ Pd under both reducing and oxidizing conditions, with the latter occurring 100× faster (Cui et al., 2004; Utsunomiya and Ewing, 2006). The compositions of the Oklo metallic aggregates differ from anthropogenic ones, however, likely due to the effects of preferential chemical leaching (Utsunomiya and Ewing, 2006). Anthropogenic UO_2 fuel pellets in light water reactors are typically clad in zircaloy or other materials, which prevents fuel interaction with the water used as a coolant and moderator. The Oklo reactors resided in a relatively open geological setting, with water and other fluids able to flow around and interact with the fuel. Uranium for anthropogenic reactor fuel is chemically purified prior to isotopic enrichment as UF_6 and oxidation to UO_2. In contrast, natural uranium deposits contain chemical impurities and often greater than %-level abundances of ingrown Pb from the α-decay of U and Th. These additional constituents can have a significant impact on the subsequent ε-phase chemistry and growth.

Isochrons derived from measurements of ^{135}Ba and ^{137}Ba (whose fissionogenic parents were ^{135}Cs ($t_{1/2} = 2.3$ Ma) and ^{137}Cs ($t_{1/2} = 30$ y), respectively) showed that the fissionogenic Ba was captured as radiocesium within five years of RZ13 criticality ceasing (Groopman et al., 2018). It was interpreted that these metallic aggregates exhibited multiple generations of crystallization and that closure did not occur until post-criticality. The ^{235}U thermal fission yields for ^{133}Cs, ^{135}Cs, and ^{137}Cs are relatively large, each approximately 6%. Neutron-capture production of ^{134}Cs ($t_{1/2} = 2.1$ y) from ^{133}Cs results in additional short-term radioactivity. Cesium is volatile and water-soluble, and can easily escape into the environment after a containment or fuel cladding failure, making its radioactive isotopes a serious potential health hazard. It should be noted that the β-decay parent of ^{135}Cs, ^{135}Xe ($t_{1/2} = 9.1$ h), has an incredibly large *n*-capture cross section ($\sigma_{c,thermal} = 2.8$ Mb, resonance integral $= 7.9$ kb), so in higher flux reactors most of it is burned up to effectively stable ^{136}Xe ($t_{1/2} = 2.2 \times 10^{21}$ y); during shutdown periods, ^{135}Cs is produced through the decays of ^{135}I ($t_{1/2} = 6.6$ h) and ^{135}Xe. In lower flux, pulsed reactors, such as the Oklo RZs, much less ^{135}Xe is burned up before its decay to ^{135}Cs.

Most metallic aggregates in RZs 10 and 13 formed between uraninite crystals (Gauthier-Lafaye et al., 1996; Groopman et al., 2018). One notable exception was found by Groopman et al. (2018), which was completely encapsulated by uraninite and therefore not in direct contact with water or other fluids. This aggregate showed a more abundant and varied accumulation of fissionogenic Cs and Ba than the inter-uraninite aggregates, evidence for Ba/Cs fractionation within the uraninite. This aggregate also shared an age relationship (for Ba and Cs closure) with the other aggregates. This revealed potential implications for the sequestration of Tc and Cs fission products within fuels. Here we present an investigation into the elemental and isotopic fractionation of

Table 1

Chemical compositions (wt.%) of metallic aggregates reported in the literature. "–" indicates unreported values.

Sample	Ru	Rh	Pd	Te	Pb	U	As	S	Bi	Sb	Ni	Cu	Total
SD37-S2/CD (RZ13)[a]	50.88	6.23	1.29	3.79	2.89	0.21	16.73	1.93	4.23	0.61	0.83	0.22	89.83
SD37-S2/CD (RZ13)[b]	33.51	4.64	–	2.71	38.89	0.39	7.99	7.43	–	–	–	–	95.55
SF29 (RZ10)[c]	25.06	4.63	–	0.7	20.51	1.42	31.29	11.62	–	–	–	–	95.32

[a] Kikuchi et al. (2010).

[b] Hidaka et al. (1999).

[c] Gauthier-Lafaye et al. (1996).

fissionogenic Tc, Ru, Cs, and Ba into metallic aggregates within RZ 13. We are specifically interested in the distributions of sequestered fissionogenic Cs and Tc within the metallic aggregates.

2. Geological setting and sample

The geological setting of the Francevillian basin, which contains the natural nuclear reactors at Oklo and Bangombé, has been described extensively elsewhere (see, e.g., Weber et al., 2016, and references therein) and was first described by Weber (1968). We therefore provide only a brief recounting here. The Francevillian basin contains a sedimentary series that is among the best preserved of its type and age in the world, dating to the Palaeoproterozoic age. On top of the Archean basement belonging to the western part of the Congo Craton, the Francevillian A (FA) formation is mainly composed of fluvio-deltaic conglomerates and sandstones up to 1000 m thick. The Oklo and Mounana uranium deposits lie at the top of this formation and are dated to 1950 ± 30 Ma (Naudet and Horowitz, 1991; Ruffenach et al., 1976). On top of the FA and uranium deposits lie FB black shales with thicknesses ranging from 400 to 1000 m. The FC-FE formations mainly consist of dolomites, black shales, banded cherts, sandstones and volcanic sediments. Within the basin, a swarm of dolerite dyke intrusions occurred during a period of 700–970 Ma ago, with relatively large uncertainties depending upon the dating method and samples used (Bonhomme et al., 1978, 1982; Evins et al., 2005; Gauthier-Lafaye et al., 1996; Holliger, 1991, 1994; Nagy et al., 1991). The most recent data puts the dolerite ages in the range of 860–890 Ma, with another Pb-loss event near 500 Ma (Evins et al., 2005). These dykes affected the retention of fission products, radionuclides, and primary uranium within the Oklo deposits.

Oklo RZ13 was singular among the natural nuclear reactor sites at Oklo and Bangombé, having the shortest duration of criticality (24.2 ka), the highest neutron flux, the highest proportion of its fission inventory resulting from ^{238}U (17.9%) and ^{239}Pu (7.2%), and the highest heat dissipation (Hidaka and Holliger, 1998). Zone 13 lies ~225 m underground and 25 m south of a dolerite dike, which likely caused episodic mobility of its fission products, Pb, and U (Gauthier-Lafaye et al., 1996; Holliger, 1991, 1994). Our sample of RZ13, from drill hole 2 in the SD.37 gallery (SD.37-S2) experienced the highest burnup, with the lowest yet found ^{235}U/^{238}U ratio of 0.365% (Groopman et al., 2018), indicating that it was sourced from the center of the reactor core (Gauthier-Lafaye et al., 1996). The ^{235}U/^{238}U ratio ranged up to 0.406% across the 3 mm × 4 mm breadth of the sample (Groopman et al., 2018). This corresponds to roughly 44–50% of the initial ^{235}U having fissioned during criticality. The uraninite grains (nominally UO_2) in this sample are cut by veins of La–Ce–Sr–Ca aluminous hydroxy phosphate (Dymkov et al., 1997; Holliger, 1994), which is unique among the RZs. Most of the aluminous phosphate, which formed during and shortly after criticality, trapped fissionogenic Xe and I in abundance, with present day concentrations of up to 3×10^{-2} cm^3 STP/g, the highest concentration ever observed in a natural mineral (Meshik et al., 2000). Excess ^{130}Xe indicated that neutron capture occurred on fissionogenic ^{129}I. The isotopic composition of the captured Xe further revealed a record of the reactor cycling on for ~30 min and off for 2.5 h over the duration of its operation (Meshik et al., 2004), with water-to-steam conversion likely providing reactivity control to prevent a runaway thermal event. This sample also provided the first *in-situ* evidence of fissionogenic Cs and Ba capture within the reactor core (Groopman et al., 2018), with fissionogenic Cs and Ba being found in association with the metallic aggregate ε-phase.

3. Methods

We characterized the isotopic and chemical distribution of fission and neutron capture products using the Naval Ultra-Trace Isotope Laboratory's Universal Spectrometer (NAUTILUS) at the U.S. Naval Research Laboratory (NRL), and the Ametek Cameca Nano-scale Secondary Ion Mass Spectrometer (NanoSIMS) 50(L) at the Carnegie Institution of Washington. Regions of interest containing Ru aggregates were identified using raster ion imaging on the NAUTILUS and by energy dispersive X-Ray spectroscopy (EDXS) mapping. We used an Oxford X-Max 80 X-ray detector on a ThermoFisher (formerly FEI) Nova 600 NanoLab DualBeam focused ion beam/scanning electron microscope (FIB/SEM) operated at 20 keV.

The NAUTILUS at NRL combines a heavily modified small-geometry Cameca ims 4f SIMS with a single-stage accelerator mass spectrometer (SSAMS), described in detail in Groopman et al. (2020). The SSAMS operates at 300 kV and acts as a molecule-filtering "detector" for the SIMS. The ims 4f may be used as a standalone SIMS, with traditional Faraday cup (FC) or electron multiplier (EM) detectors, or the secondary ions may be deflected into the SSAMS. Following acceleration in the SSAMS, the secondary ion beam with a single mass-to-charge ratio (m/z) transits a gas filled cell, where collisions between the ions and the gas cause molecular isobars to be dissociated. The resulting atomic ion and molecular fragment ion beams are subsequently filtered by m/z in the SSAMS and atomic ions are detected with an EM. Since the SSAMS may accept positive ions, unlike traditional tandem AMS instruments, the NAUTILUS achieves an increase in sensitivity to electropositive elements of several orders of magnitude relative to its cousin SIMS-AMS hybrid instruments, e.g., (Christl et al., 2013; Freeman et al., 1994; Mao et al., 2008). The NAUTILUS is a single-collector SIMS-like instrument, though measurements on each of the individual detectors may be interleaved during an analysis. The instrument uses synchronized electrostatic peak switching (EPS) on its two magnetic sectors (Groopman et al., 2017) to select masses within a ±6.5% range of each magnet's field-tuned m/z. EPS works by biasing the otherwise electrically insulated flight tubes through each magnetic sector, which alters the ions' energies within the sectors and therefore their curvature radii (Adriaens and Adams, 1991; Slodzian et al., 1984).

Using the NAUTILUS, we collected raster ion images of several Ru metal aggregates and the surrounding matrix, with image sizes between 100 and 150 μm square (64–128 pixels square, respectively). Images were collected using a 1 nA O^- probe from the duoplasmatron ion source, with two analyses performed at each location. The first analysis consisted of raster ion images of ^{99}Ru$^+$, ^{100}Ru$^+$, ^{101}Ru$^+$, ^{102}Ru$^+$, ^{103}Rh$^+$, ^{104}Ru$^+$, ^{105}Pd$^+$; the second consisted of ^{133}Cs$^+$, ^{134}Ba$^+$, ^{135}Ba$^+$, ^{136}Ba$^+$, ^{137}Ba$^+$, and ^{138}Ba$^+$, all with count times of 45 s per frame, per isotope. Barium titanate ($BaTiO_3$) powder, alloys of Pd:Ru and Pd:Rh metal, and NIST SRM 610 glass were used as analytical standards. NIST 610 glass was used to calculate the relative sensitivity factor (RSF) between Cs and Ba, since we did not have a good matrix-matched standard for metallic aggregates that contained Cs and Ba. The RSF represents the relative ionized yield of two elements from a particular matrix. Uranium (235, 238), thorium (232), and lead (204, 206, 207, 208) isotope imaging and spot measurements were also performed on nearby uraninite and galena crystals. Likewise, we did not have an adequate uraninite standard for measuring U, Th, and Pb RSFs, so we did not construct inter-element concordia diagrams.

Following NAUTILUS analyses, we collected isotope images from different aggregates using the NanoSIMS. Five magnetic field settings and seven detectors were used per analysis to measure: (1) ^{32}S$^+$, ^{75}As$^+$, ^{99}Ru$^+$, ^{102}Ru$^+$, ^{133}Cs$^+$, ^{136}Ba$^+$, ^{206}Pb$^+$; (2) –, –, –, –, –, –, ^{207}Pb$^+$; (3) –, –, ^{100}Ru$^+$, ^{103}Rh$^+$, ^{134}Ba$^+$, ^{137}Ba$^+$, ^{208}Pb$^+$; (4) –, –, –, –, ^{135}Ba$^+$, ^{138}Ba$^+$, ^{209}Bi$^+$; (5) –, –, ^{101}Ru$^+$, ^{104}Ru$^+$, –, –, – (where "–" indicates no measurement on a trolley for that magnetic field). It would have been possible to alternatively measure Pd and Ag isotopes in the above setup, however we were not aware (until after the analyses were complete) of the means to set unique voltages to the detector ESAs for each magnetic field setting on the NanoSIMS. Adjusting the individual ESA voltages in addition to the deflector plates for each magnetic field would have allowed the additional masses to be analyzed. In the future, the acquisition setup could be: (1) ^{32}S$^+$, ^{99}Ru$^+$, ^{102}Ru$^+$, ^{105}Pd$^+$, ^{133}Cs$^+$, ^{136}Ba$^+$, ^{206}Pb$^+$; (2) –, –, –, –, –, –, ^{207}Pb$^+$; (3) –, ^{100}Ru$^+$, ^{103}Rh$^+$, ^{106}Pd$^+$, ^{134}Ba$^+$,

^{137}Ba^{+}, ^{208}Pb^{+}; (4) –, –, –, –, ^{135}Ba^{+}, ^{138}Ba^{+}, ^{209}Bi^{+}; (5) –, ^{101}Ru^{+}, ^{104}Ru^{+}, ^{107}Ag^{+}, –, –, –. Lead-204 was not measured on the NanoSIMS. Implementing the magnet-jumping multicollection setups above (which Cameca calls "combined mode") were not trivial, and were the iterative result of several attempts to use fewer magnetic field settings and different arrangements of the detector trolleys. At the time, ^{204}Pb was not deemed sufficiently important to the primary investigation of the behaviors of Cs, Ba, and Tc, though it could be added to future analyses. Isotope images were collected from 25 μm square regions (256 px × 256 px), counting for 131 s/frame and waiting 2 s between magnetic field jumps, using a 140 pA O^{-} primary probe from the Hyperion-II ion source.

Isotope image data were processed using the in-house software package NAUTILimage (Evan Groopman, NRL) for both NAUTILUS and NanoSIMS data, and L'Image (Larry Nittler, Carnegie Institution) for NanoSIMS data. The NAUTILimage software propagates all statistical uncertainties on a per-pixel basis, including for arbitrary image math, such as when one calculates the fissionogenic component of an isotope, e.g., $^{138}\text{Ba}^{*} = {}^{138}\text{Ba}_{\text{measured}} - ({}^{138}\text{Ba}_{\text{terrestrial}}/{}^{136}\text{Ba}_{\text{terrestrial}}) \times {}^{136}\text{Ba}_{\text{measured}}$. Many of the features of NAUTILimage were inspired by L'Image capabilities. Depth profiles and isotope ratios from spot measurements were calculated using other in-house software, NAUTILsiphon (Evan Groopman, NRL). Likewise, cycle-by-cycle error propagation and arbitrary isotope math were used during analysis, in addition to other standard depth profiling considerations, such as time interpolation. Both programs also allow the mean values and uncertainties of isotope ratios to be calculated in several ways, to investigate potential ratio bias and/or the appropriate magnitude of the uncertainties. The means and uncertainties can be calculated using Poisson statistics (total counts), the mean and standard deviation or standard error, the Beale estimator (Ogliore et al., 2011), weighted mean, biweighted mean and scale (Beers et al., 1990), and bootstrap resampling using the bias corrected accelerated (BCa) algorithm (Efron and Tibshirani, 1986).

Linear regressions were performed on three-isotope plot data to determine neutron fluence or to construct isochrons, using the method of York et al. (2004). The Python code to perform these fits is provided in the Appendix under a permissive BSD-3 license. The code also calculates the mean squared weighted deviation (MSWD) of the fit and its associated uncertainty, following the description by Wendt and Carl (1991). The regression provides an x-axis intercept and uncertainty, which matches the value of the conventional intercept when the axes are transposed. The code also generates confidence and prediction intervals at a user-specified level (e.g., 95%) for the regression, which can be calculated at the data x-values, or for the former at any array of user-provided values. All 2σ uncertainties reported in this paper were calculated using the 95% confidence level of the Student's t-distribution quantile function with N-2 degrees of freedom (where N is the number of data points); they are not simply the 2× the fit parameter uncertainty, which is an underestimate for $N \lessapprox 62$.

The Python code also contains functions for calculating a 1D kernel density estimate (KDE) that weights the uncertainty for each data point. Many KDE estimation methods (and software libraries) select a uniform bandwidth for all data. This assumption is not appropriate for most SIMS isotope ratio data, where the uncertainties are driven largely by the number of counts in a given measurement. The provided functions model each data point as a Gaussian distribution with mean and standard deviation equal to the datum value and uncertainty, respectively. At each user-defined location (across the range to evaluate the KDE), the contributions from each Gaussian distribution are summed. This method is used in several figures in this paper where it can be difficult to distinguish clusters of data and their error ellipses. This method could be generalized to other kernel shapes and to 2D data with (optionally) correlated uncertainties.

4. Results

Isotope and isotope ratio images are shown in Figs. 1–5 and Figs. A2, A3, A5 and A6 from the two NAUTILUS and two NanoSIMS fields of view (FOV). Isotope image intensities are shown in counts·second^{-1} (cps). Isotope and ratio images with a charge state shown (+) indicate that no RSF was applied to the isotope or ratio; labels without a charge state have had an RSF applied. RSFs were measured from available standards. As is typical for SIMS, exact matrix-matching was not possible between sample and standards, so some small matrix effects may not be accounted for between elements. Color bars on the isotope ratio images show the terrestrial and ^{235}U fission yield values (where applicable) as a blue right arrow and a green left arrow, respectively. These values assume no chemical fractionation or burnup of parent radioisotopes. All of the Ru and Rh in the reactors, and the vast majority of Pd, is fissionogenic, so no corrections were made for primordial or admixed material (Curtis et al., 1989; Hidaka and Holliger, 1998; Hidaka et al., 1993b). There exists considerable terrestrial Ba and Cs in the reactor, so Ba isotope ratio images show the ^{i}Ba*/^{136}Ba values, where $^{i}\text{Ba}^{*} = ({}^{i}\text{Ba}_{\text{sample}} - ({}^{i}\text{Ba}_{\text{standard}}/{}^{136}\text{Ba}_{\text{standard}}) \times {}^{136}\text{Ba}_{\text{sample}})$ is the fissionogenic component of the isotope. Stable Cs is monoisotopic, so no corrections were made. However, stable ^{133}Cs is also a major component of the fission products, ~6.8% of the total yield at RZ13 (Hidaka and Holliger, 1998).

4.1. NAUTILUS FOV #1

Fig. 1 shows the isotope images for m/z 99–105 (Ru, Rh, Pd), and m/z 133–138 (Cs, Ba) from NAUTILUS FOV #1. This FOV includes a metallic aggregate in the center-left region, which is highlighted by a dashed, white contour based on the ^{101}Ru^{+} intensity, for visual clarity. In the aggregate, Ru is approximately 20× and 1000× more abundant than Rh and Pd, respectively (once an RSF is applied). Rhodium and palladium are relatively more abundant in smaller metal-rich regions on the center-right of the FOV, being ~10% and 1% of the Ru abundance. This compares to bulk abundances in RZ13 where Ru is 4.2× and 5.3× more abundant than Rh and Pd (Hidaka and Holliger, 1998). From this and EDXS analysis of RZ13, it is apparent that more Rh and Pd are retained in the uraninite relative to Ru. Ruthenium-99 and 100 do not correlate perfectly with other Ru isotopes, potentially indicative of Tc fractionation and *n*-capture. Cesium-133 is most highly concentrated within the aggregate, whereas a majority of the Ba signal in this FOV is concentrated outside. Fissionogenic isotopes with radio-Cs parents, particularly ^{135}Ba and ^{137}Ba, are relatively more abundant than shielded ^{136}Ba within the aggregate, indicative of live ^{135}Cs and ^{137}Cs sequestration, as in Groopman et al. (2018).

Fig. 2 shows the isotope ratio images including the white, dashed contour based upon the ^{101}Ru^{+} signal. The ^{99}Ru/^{101}Ru and ^{100}Ru/^{101}Ru ratio images within the aggregate are heterogeneous, with values ranging from the expected fission yield to more enriched in ^{99}Ru and ^{100}Ru at the center of the aggregate. The ^{102}Ru/^{101}Ru and ^{104}Ru/^{101}Ru isotope ratios are visually homogeneous within the aggregate. The ^{105}Pd/^{101}Ru ratio shows a small enrichment collocated with enhanced ^{99,100}Ru at the aggregate center. The ^{103}Rh/^{101}Ru ratio is also slightly heterogeneous, with more Rh being concentrated in the right-most lobe of the aggregate. Cesium-133 is highly correlated with the ^{134}Ba*/^{136}Ba, ^{135}Ba*/^{136}Ba, and ^{137}Ba*/^{136}Ba ratios, indicative of live radio-Cs capture. Fissionogenic ^{138}Ba* is also concentrated in the metallic aggregate, as has previously been observed (Groopman et al., 2018). Both Ba and Cs isotopes are less abundant in the right-most lobe of the aggregate, a potential indication that phases more amenable to Rh and Pd are less likely to sequester Cs. The Pd- and Rh-enriched phases at the center-right of the FOV similarly do not show evidence for enhanced Cs or Ba* content.

It is notable that the highest enrichments in ^{99}Ru/^{101}Ru, due to the preferential sequestration of ^{99}Tc, are anti-correlated with the enrichments in Cs and Ba* isotopes. This pattern is consistent across all

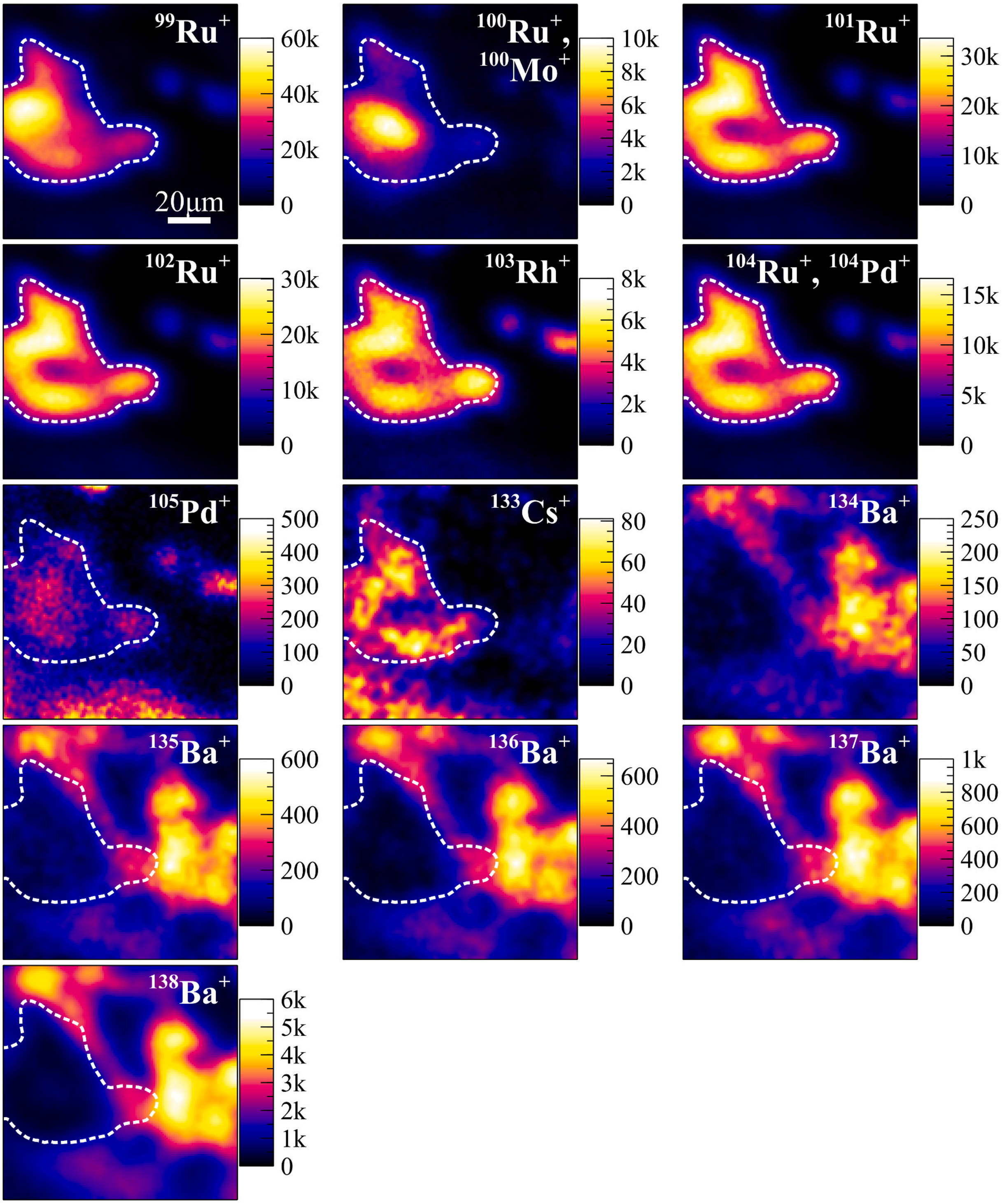

Fig. 1. Isotope images from NAUTILUS FOV #1. The metallic aggregate is in the center-left of the frame with a white, dashed outline for visual clarity. Intensities are in counts·s^{-1} (150 μm × 150 μm).

NAUTILUS and NanoSIMS FOVs. Both enrichments and depletions in these sequestered fission products are present in the Ru-rich metallic aggregates, however it seems likely that they segregated into different phases and/or did so at different times. The correlated presence of ^{100}Ru and positive Δ^{99}Ru values indicates that most *n*-capture on ^{99}Tc occurred after Tc was sequestered within the growing aggregate (where Δ^{99}Ru is the deviation in percent of the measured value relative to the standard, $\Delta^{99}\text{Ru} = 100 \times [(^{99}\text{Ru}/^{101}\text{Ru})_{\text{measured}}/(^{99}\text{Ru}/^{101}\text{Ru})_{\text{standard}} - 1]$). If most *n*-capture occurred while Tc was mobile within the uraninite or bound in other phases, we would expect ^{100}Ru to have been more evenly distributed with the other Ru isotopes within the aggregates.

4.2. NAUTILUS FOV #2

Fig. A2 shows the isotope images for m/z 99–105 (Ru, Rh, Pd), and 133–138 (Cs, Ba) from NAUTILUS FOV #2. A dashed, white contour from the ^{101}Ru^{+} signal is also shown in several panels. The Ru and Rh isotopes are generally well correlated in this FOV, however, there are

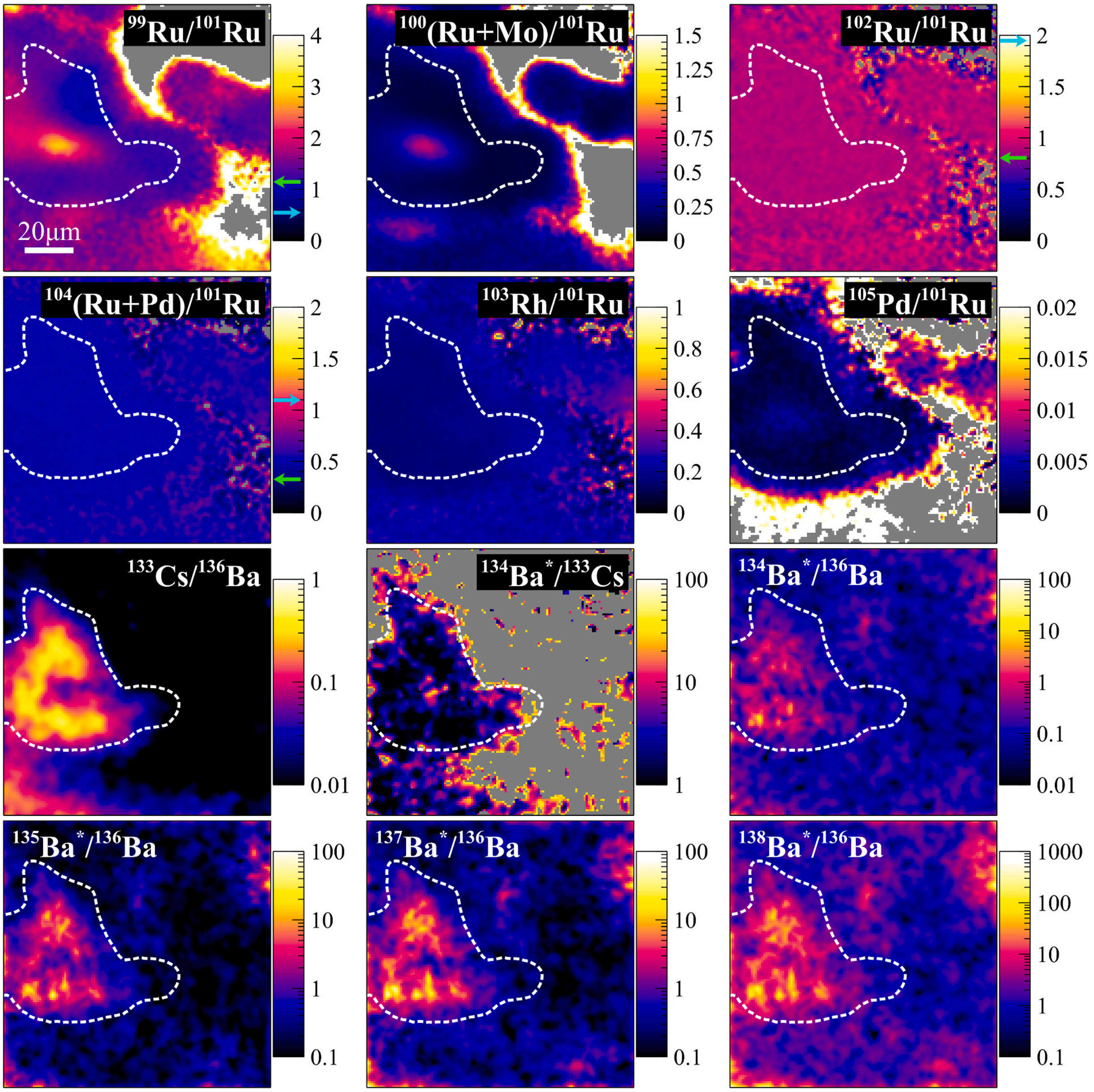

Fig. 2. Isotope ratio images from NAUTILUS FOV #1. The metallic aggregate contains correlated excesses in ^{99}Ru (extinct ^{99}Tc) and ^{100}Ru, and fissionogenic Cs and Ba throughout. Ruthenium-99 is anti-correlated to the presence of Cs and Ba*. Grey regions are masked by thresholding the ^{101}Ru$^+$ signal where counts were very low. (150 μm × 150 μm)

several additional features in the ^{100}Ru$^+$ panel that are likely due to an isobaric interference from ^{100}Mo$^+$. We did not simultaneously measure another isotope of Mo, so we cannot correct for the inferred ^{100}Mo contribution. The ^{99}Ru$^+$ image exhibits several features that are not matched by the other Ru isotopes, again indicative of Tc/Ru fractionation. A couple of Pd-rich grains are present outside the perimeter of the outlined aggregate. The Cs and Ba isotope images were collected in a separate session from the Ru, Rh, and Pd isotopes. The FOV selected for Cs and Ba images was inadvertently set to be 100 μm on a side instead of 150 μm, and 64 px square instead of 128. The Cs and Ba images shown were resampled to a resolution to 128 px/150 μm and padded by 25 μm on a side (padded area shown in grey). The Cs$^+$ signal appears to be most highly correlated with Ru and Rh in the center of the aggregate, whereas the Ba$^+$ signals are concentrated along the upper region of the aggregate.

Fig. A3 show the isotope ratio images for NAUTILUS FOV #2. A vein of enriched ^{99}Ru/^{101}Ru is visible within the aggregate and in much of the uraninite to the left of and below the dashed outline. The ^{99}Ru/^{101}Ru ratio is high on the left side of the FOV in the surrounding uraninite where the ^{101,102,104}Ru isotope abundances are low. The lower tip of the aggregate also contains a large enrichment in ^{99}Ru/^{101}Ru. The intense spots in the ^{100}(Ru + Mo)/^{101}Ru ratio image outside of the aggregate outline are likely due to Mo-rich phases. The ^{133}Cs/^{136}Ba and ^{134,5,7,8}Ba*/^{136}Ba images are strongly correlated within the aggregate once more.

4.3. NanoSIMS FOV #1

Fig. 3 shows isotope images of m/z 32, 75, 99–104, 133–138, 206–209 from NanoSIMS FOV #1, while Fig. 4 shows the isotope ratio images. Visible within the FOV is the metallic aggregate surrounded by several uraninite grains and a region of aluminous phosphate in the upper left. The aluminous phosphate can be identified from the high Ba concentration in Fig. 3 correlated with the presence of Si, Al, increased

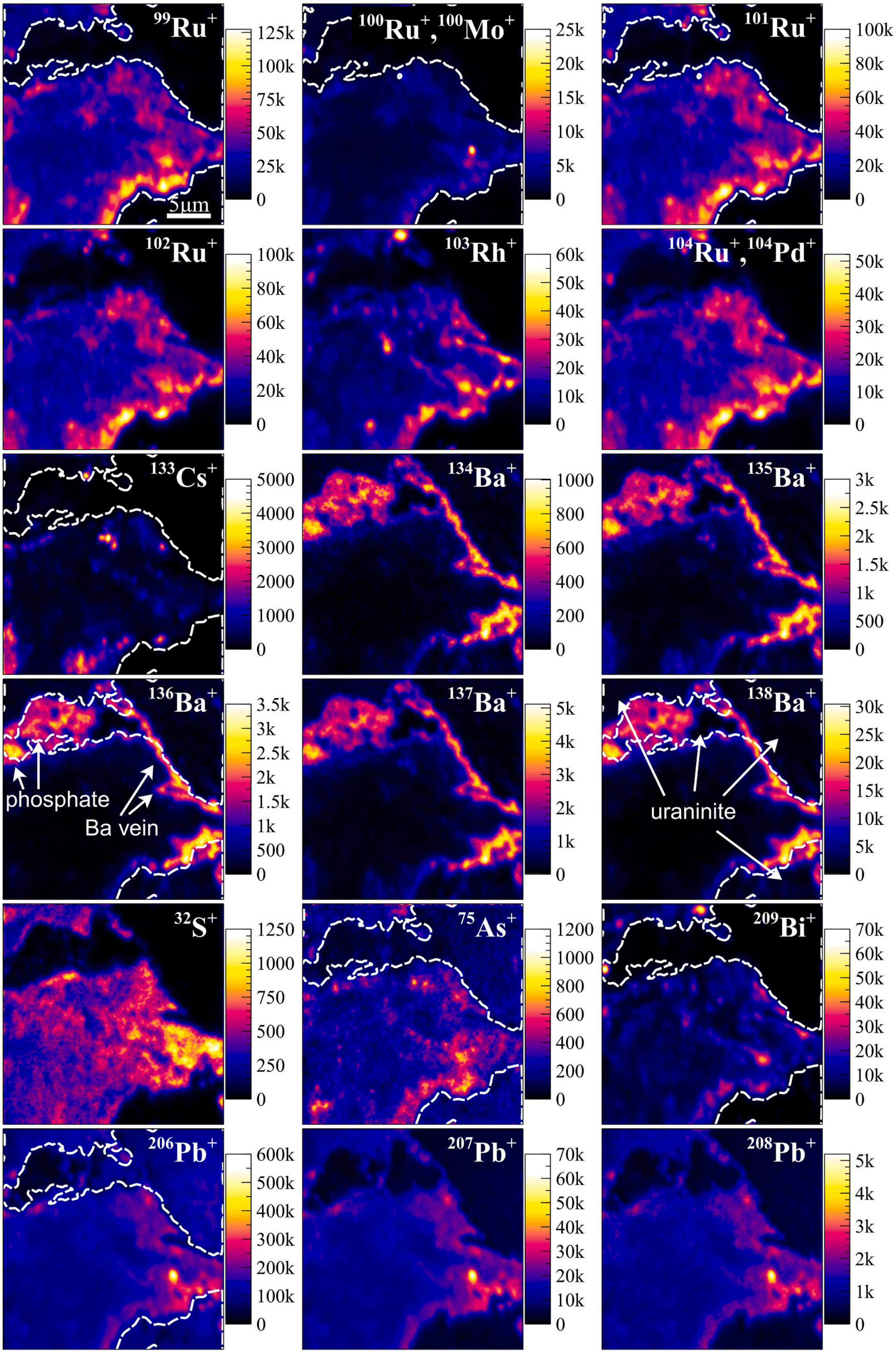

Fig. 3. Isotope images from NanoSIMS FOV #1 (25 µm × 25 µm).

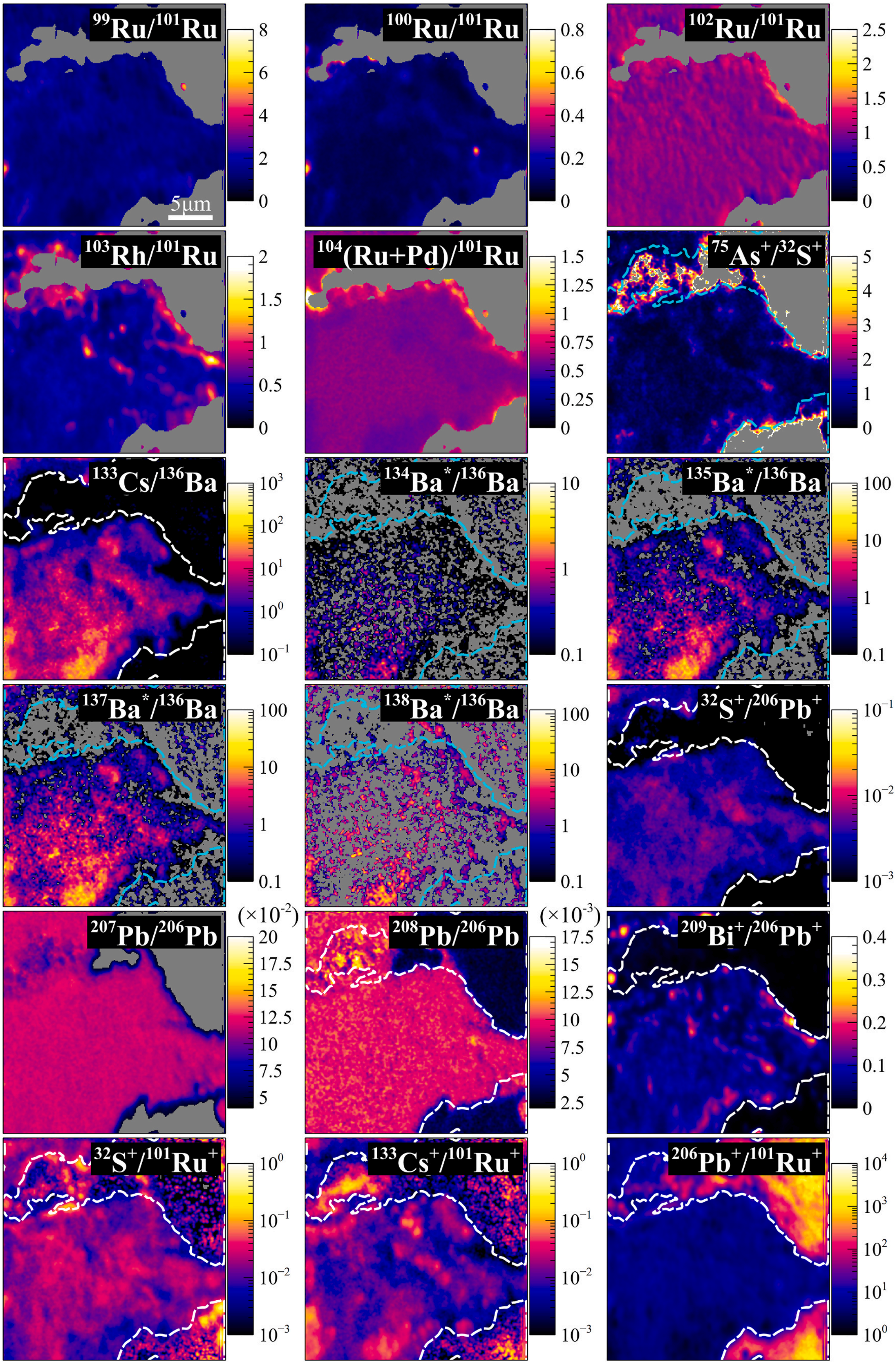

Fig. 4. Isotope ratio images from NanoSIMS FOV #1 (25 μm × 25 μm).

O, and decreased U in Fig. A4. Fig. 3 shows a thin vein of Ba-rich material between the metallic aggregate and the uraninite grains. This is not aluminous phosphate since it corresponds to a region of depleted Al and Si in Fig. A4. Secondary ion yields in SIMS are sensitive to the work function of the sample surface, which can be affected by the chemical composition, crystallographic orientation, and the variable sputter rate of different grains; the NanoSIMS, in particular, can be especially sensitive to topographic and sample tilt effects. Therefore, caution is required when interpreting a solitary ion signal, e.g., $^{32}S^{+}$ in Fig. 3, which appears to show a gradient in S content across the width of the FOV. Taking the ratio of $^{32}S^{+}$ to another isotope, e.g., $^{101}Ru^{+}$ or $^{206}Pb^{+}$ as in Fig. 4, shows a more uniform image dominated by local structure rather than a global left-right intensity trend.

Fig. 4 shows many isotope ratios images where correlations are qualitatively visible. The ratio images $^{102}Ru/^{101}Ru$, $^{207}Pb/^{206}Pb$, and $^{208}Pb/^{206}Pb$ are all uniform in the aggregate, since there should have been negligible chemical fractionation between the short-lived parent isotopes of each. Both $^{207}Pb/^{206}Pb$ and $^{208}Pb/^{206}Pb$ ratios are higher within the aggregate than in the surrounding uraninite. Common Pb has been found to be underabundant in the aggregates ($^{204}Pb/^{206}Pb < 0.0002$), so nearly all of the Pb is radiogenic in origin (Gauthier-Lafaye et al., 1996; Kikuchi et al., 2010), and therefore $^{207}Pb/^{206}Pb \sim {}^{207}Pb^{*}/^{206}Pb^{*}$. The measured $^{207}Pb/^{206}Pb$ and $^{208}Pb/^{206}Pb$ ratios in the aggregate are 0.1139 (15) and 0.0095 (3), respectively, where the number in parentheses is the 2σ uncertainty on the last significant digit (s). In contrast, the $^{207}Pb/^{206}Pb$ and $^{208}Pb/^{206}Pb$ ratios in the surrounding uraninite range between 0.0365–0.0418 and 0.0030–0.0033, respectively. Elevated $^{208}Pb/^{206}Pb$ outside of the aggregate outline was likely due to the increased presence of common Pb (see Section 5.5.5).

The ratios of $^{134,5,7,8}Ba^{*}/^{136}Ba$, $^{133}Cs/^{136}Ba$, and $^{133}Cs/^{101}Ru$ are all highly correlated. Ruthenium-99 and -100 relative to ruthenium-101 are generally correlated, aside from a small intense m/z 100 region in the center-right of the FOV. This may be due to a small Mo-rich phase. Regions with the largest excesses in Ba* and Cs appear anti-correlated with $^{32}S^{+}/^{101}Ru^{+}$. Slight depletions in the $^{104}(Ru + Pd)/^{101}Ru$ ratio appear to correlate with depleted $^{99}Ru/^{101}Ru$, while being in the locations with the lowest Ba* and Cs abundances. Fig. 5 shows an RGB image composed of $^{99}Ru/^{101}Ru$ (red), $^{135}Ba^{*}$ (green), and ^{133}Cs (blue) images, whose intensities have been scaled to their individual maxima. This image shows the distinct correlation between Ba* and Cs. The largest abundances of Ba* and Cs occur where the $^{99}Ru/^{101}Ru$ ratio is lowest. Likewise, there is very little Ba* and Cs where the $^{99}Ru/^{101}Ru$ indicates higher Tc sequestration. It is therefore apparent that fissionogenic Tc and Cs preferentially segregated into different aggregate phases prior to their decay.

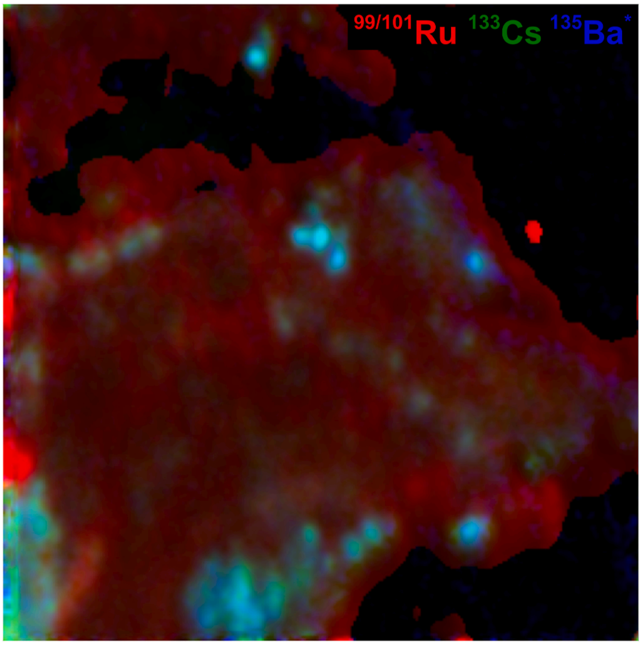

Fig. 5. RGB image of $^{99}Ru/^{101}Ru$ (red), $^{133}Cs^{+}$ (green), $^{135}Ba^{*+}$ (blue), from NanoSIMS FOV #1. Cesium and fissionogenic Ba are highly correlated. The highest concentrations of Cs and Ba are located where $^{99}Ru/^{101}Ru$ is lowest. Fissionogenic Tc and Cs therefore partitioned into different phases.

Fig. A4 shows the post-NanoSIMS EDXS maps of FOV #1. The SEM FOV was set slightly larger than the NanoSIMS sputter crater, which is visible in the SE image (upper left) and outlined in the EDXS images. Individual image intensities have been rescaled for visual clarity. Qualitatively, Ru and Rh signals appear to be more intense in the regions containing excess Cs. These regions are somewhat more depleted in S, As, and Pb than others within the aggregate indicating that Cs may prefer more noble metal-rich phases. Palladium is more abundant in the uraninite than in the aggregate, potentially due to preferential loss with Mo, or just superior retention in UO_2.

4.4. *NanoSIMS FOV #2*

Isotope and ratio images from NanoSIMS FOV #2 are shown in Fig. A5 and Fig. A6 (25 μm × 25 μm). A pair of aggregates are visible in the upper left of the FOV. Barium- and lead-rich materials are present in the remainder of the FOV, and in the upper middle, a sulfurous vein is present. Cesium is primarily concentrated in the lower-left of the two aggregates, whereas Rh and Bi are more concentrated in the upper one. Intense spots of ^{99}Ru and ^{100}Ru are visible and collocated. Outside of the outlined aggregates, m/z 100 is less intense but visible, and is likely ^{100}Mo. Similar to the other FOVs, Cs and Ba* isotopes are found to be collocated, though $^{138}Ba^{*}$ is underabundant in this FOV and more difficult to distinguish from the low-count background. The two main aggregates differ slightly in their Ba* isotopic compositions, with the upper aggregate containing relatively more $^{137}Ba^{*}$ relative to Cs or other Ba* isotopes. Based upon $^{207}Pb/^{206}Pb$ and $^{208}Pb/^{206}Pb$ ratios, the sulfur-rich vein, including what is likely galena, contains Pb with an older apparent age than the metallic aggregates. The Ba-rich regions outside of the metallic aggregates and S-vein show more recently disturbed Pb contents, with lower $^{207}Pb/^{206}Pb$ and $^{208}Pb/^{206}Pb$ ratios.

4.5. *Combined NAUTILUS and NanoSIMS data*

4.5.1. *Ru & Tc*

The half-life of ^{99}Tc ($t_{1/2} = 0.21$ Ma) is 10× longer than the estimated duration of RZ13 criticality (24 ka). Therefore, nearly 99% of the ^{100}Ru in the reactor was produced by neutron capture on ^{99}Tc ($\sigma_{c,\ 99Tc} = 23.6 + 324{\cdot}r$ barns), with the remaining 1% from ^{99}Ru ($\sigma_{c,\ 99Tc} = 7.3 + 171{\cdot}r$ barns), based upon the average flux and hardness ($r = 0.241$) of the neutron spectrum reported by Hidaka and Holliger (1998). Fig. 6 shows the correlation of $^{100}Ru/^{101}Ru$ with $^{99}Ru/^{101}Ru$, where the range of $^{99}Ru/^{101}Ru$ above and below the fission yield line was due to fractionation of ^{99}Tc within the reactor and metallic aggregate phases. This range spans nearly an order of magnitude, and most points demonstrate fractionation favoring Tc. Two linear regressions are shown, one for data from the NAUTILUS FOV #1 (red diamond symbols), and one for the NanoSIMS FOVs (green triangle markers). The linear regressions return slopes, intercepts, and MSWDs of: 0.122(3), -0.023(5), and 48(1), respectively, for the NAUTILUS data; and 0.077(6), -0.014(7), and 7.8 (4) for the NanoSIMS data. Excess scatter about the regression line may be due in part to the presence of ^{100}Mo (data from NAUTILUS FOV #2 were omitted from this plot due to the inferred presence of Mo around this aggregate – see Fig. A2). However, were there a significant presence of ^{100}Mo, we would expect the $^{100}Ru/^{101}Ru$ intercepts to be positive, which is not the case (i.e., the presence of $m/z = 100$ signal that was not due to neutron capture). The uncertainties on the NAUTILUS data, primarily from counting statistics, appear to be underestimated, as they do

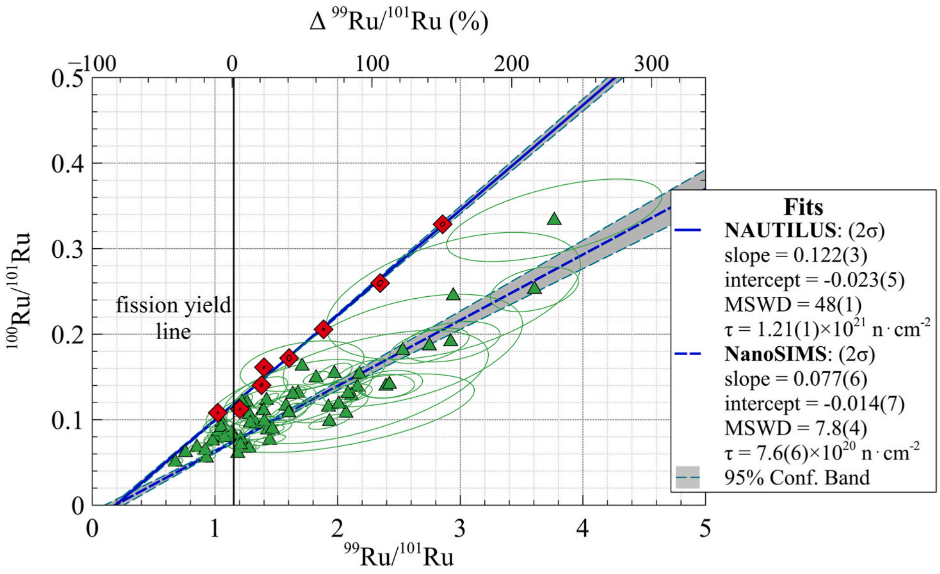

Fig. 6. ^{99}Ru/^{101}Ru vs. ^{100}Ru/^{101}Ru from NAUTILUS (red diamonds) and NanoSIMS (green triangles) data from which neutron fluences of 1.2 × 10^{21} and 7.6 × 10^{20} n·cm^{-2} were calculated, respectively. These match the range of literature values for RZ13. The difference in fluence may be reflected by the difference in size between the aggregates imaged, 75 μm for the NAUTILUS and 10–20 μm for the NanoSIMS. Some excess scatter may be due to the presence of ^{100}Mo, which was not corrected for. (For interpretation of the references to color in this figure legend, the reader is referred to the Web version of this article.)

not fully explain the scatter about the regression. The neutron fluences from the two regression lines were estimated to be 1.21(1) × 10^{21} n·cm^{-2} and 7.6(6) × 10^{20} n·cm^{-2} for the NAUTILUS and NanoSIMS aggregates, respectively. These values agree with previous estimates for RZ13: 1.1 × 10^{21} n·cm^{-2}, based on Xe isotopes from this sample (Meshik et al., 2000); and 7.8 × 10^{20} n·cm^{-2} based on Nd isotopes in other samples from the same drill core (Hidaka and Holliger, 1998). The range shown here may reflect the difference in sizes between the measured aggregates (75 μm for NAUTILUS, 10–20 μm for the NanoSIMS), and therefore, potentially their age. The strong spatial correlation between ^{100}Ru and ^{99}Ru (^{99}Tc) is indicative of neutron capture on Tc when it was bound within the aggregates. Otherwise, ^{100}Ru would be expected to be more uniformly distributed in the aggregates like the other Ru isotopes.

4.5.2. *Cs & Ba*

Based upon in situ spot analyses, Groopman et al. (2018) identified that fissionogenic ^{135}Ba* and ^{137}Ba* were collocated with metallic aggregates, and that these isotopes were likely sequestered as live ^{135}Cs ($t_{1/2}$ = 2.3 Ma) and ^{137}Cs ($t_{1/2}$ = 30 y). The ^{137}Ba*/^{138}Ba* and ^{135}Ba*/^{138}Ba* ratios from all spot measurement were collinear, indicating that they shared an age relationship. This was interpreted as fissionogenic Cs and Ba having been sequestered within 5 years of the end of criticality. Fig. 7 shows these data (white circles) with the addition of NAUTILUS and NanoSIMS image data from this work (red diamonds and green triangles, respectively). The updated linear regression yields a slope = 0.889(18), intercept = 0.076(14), and MSWD = 1.7(4) – all uncertainties 2σ. The slope and intercept of the regression correspond to ages of 1.7(8) and 3.7(8) years, respectively, yielding a mean age of 2.7(0.6) years. We confirm that isotopes with m/z 135 and 137 behaved predominantly as radiocesium prior to their incorporation into the metallic aggregates. In blue distributions along each axis are 1D KDEs, with each data point weighted by its uncertainty. Most data have ^{135}Ba*/^{138}Ba* and ^{137}Ba*/^{138}Ba* ratios less than 0.5. The Tukey biweight location (robust mean) and scale (robust standard deviation) of the data points on each axis are 0.42 ± 0.40, though each distribution is skewed with a tail towards larger values. Since ^{135,7,8}Ba* all have similar fission yields, values less than ~1 are indicative of fractionation favoring the retention of Ba over Cs within the reactor and/or in the metallic aggregates. The NanoSIMS data tend to deviate more from the regression line (though have larger uncertainties), which may be indicative of a small amount of fractionation between ^{137}Cs and ^{137}Ba that is only visible at the smaller size scales of the NanoSIMS regions of interest (ROIs). We cannot, however, rule out the presence of a molecular isobar at m/z 137 for the NanoSIMS data.

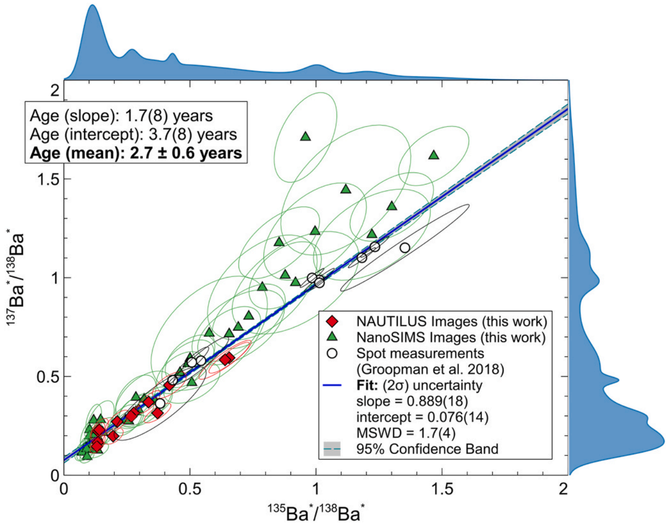

Fig. 7. Isochron between ^{135}Ba*/^{138}Ba* and ^{137}Ba*/^{138}Ba* yielding an updated age of 2.6 ± 0.6 years. Weighted 1D KDEs are shown on each axis.

Fig. 8 shows the ratios of ^{133}Cs$^+$/^{101}Ru$^+$ and ^{134,5,7}Ba*$^+$/^{101}Ru$^+$ relative to ^{138}Ba*$^+$/^{101}Ru$^+$. Ruthenium-101 was chosen as a reference isotope because many ROIs had low ^{136}Ba abundances whereas ^{101}Ru was present throughout the aggregates. The two columns show the same data but on linear (left) and logarithmic (right) scales for visual clarity (the linear scale spans a smaller range containing most data points). Data are from each FOV are color-coded: NAUTILUS FOV#1 (blue squares), FOV#2 (green diamonds), NanoSIMS FOV #1 (red circles), FOV #2 (purple triangles). Note: the ^{133}Cs$^+$/^{101}Ru$^+$ ratio was adjusted for the measured Cs/Ba RSF, however all of the other isotopes were measured as Ba$^+$, so no adjustment was necessary. We do not have reliable Cs/Ru or Ba/Ru RSF values, but these only shift the data points on a slope = 1 line and do not affect trends. The solid black lines show the expected fission yield for each 3-isotope plot.

Since ^{138}Ba* is essentially a direct fission product, the parameterization in Fig. 8 illustrates the range of chemical fractionation between Cs and Ba in the different FOVs. Rows 1, 2, and 4 show the behaviors of ^{137}Ba* (^{137}Cs, $t_{1/2}$ = 30 y), ^{135}Ba* (^{135}Cs, $t_{1/2}$ = 2.3 Ma), and ^{133}Cs relative to ^{138}Ba*. Here there is clear evidence of Ba/Cs fractionation,

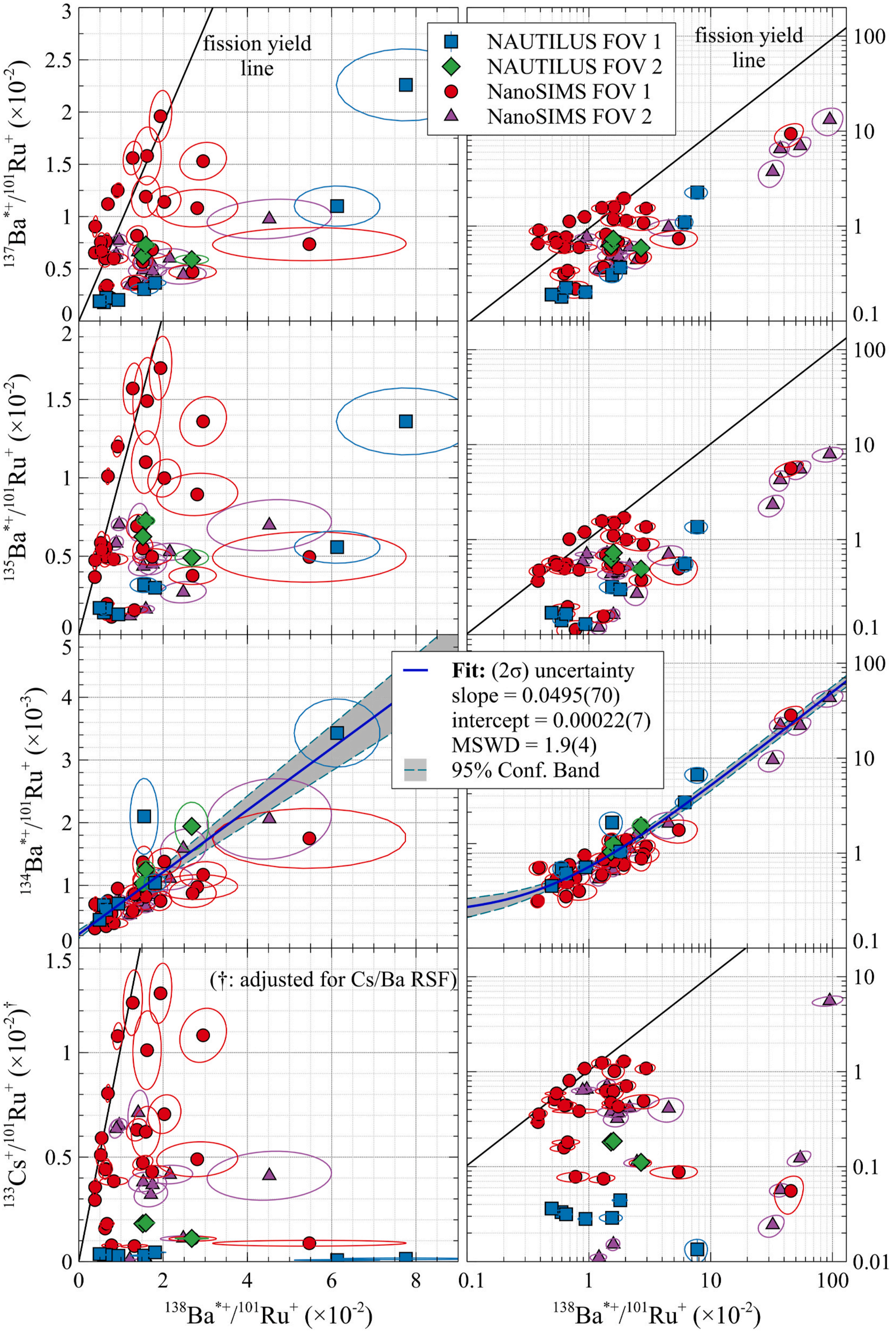

Fig. 8. ^{138}Ba*$^{+}$/^{101}Ru^{+} vs Cs and Ba* on linear (left) and log (right) scales for each FOV. ^{134}Ba*$^{+}$/^{101}Ru^{+} and ^{138}Ba*$^{+}$/^{101}Ru^{+} are correlated, indicating that most ^{134}Ba* behaved like Ba instead of Cs. Fissionogenic ^{135}Ba and ^{137}Ba behaved like Cs.

both within individual metallic aggregates, and between aggregates separated by up to 1 mm within the sample. Most points lie below the fission yield lines. For these ROIs, the ^{138}Ba* abundances are larger than ^{135,7}Ba*, indicating that Ba was preferentially sequestered in these regions and/or that Cs was preferentially lost from these localities. Several points from the NanoSIMS ^{133}Cs data lie along the fission yield line, indicating that little fractionation took place in these regions. Since isotopes with m/z 133, 135, and 137 were all expected to behave predominantly as Cs, it is possible that NanoSIMS ^{137}Ba*/^{101}Ru ratios above the fission line were due to the presence of a molecular isobar at m/z

137, whose intensity could vary spot-to-spot with the phase composition. The excesses in ^{137}Ba* could also be due to a small fraction of decayed ^{137}Cs that was preferentially sequestered as Ba. On the other extreme, locations in NAUTILUS FOV #1 tended to have the lowest Cs abundances and exhibited the highest level of Cs/Ba fractionation. Qualitatively, these data show a depletion in ^{135,7}Cs relative to the expected fission yield of >80%. In this FOV, ^{133}Cs is highly depleted and does not vary relative to ^{138}Ba*, making it difficult to draw firm conclusions. One possibility is that Cs was released from this aggregate during the intrusion of a dolerite dyke swarm 860 Ma ago (long after ^{135,7}Cs decayed to ^{135,7}Ba) approximately 15 m from RZ13 (Evins et al., 2005; Gauthier-Lafaye et al., 1996). However, this explanation is highly speculative and does not adequately explain the fractionation patterns from the other FOVs without knowing more about the specific mineralogies of the ROIs in question. As described previously, this aggregate is also larger and experienced a higher fluence than the aggregates analyzed using the NanoSIMS.

The third row in Fig. 8 shows ^{134}Ba*/^{101}Ru vs. ^{138}Ba*/^{101}Ru where the data fall along a linear trendline with slope = 0.0495(70), intercept = 0.00022(7), and MSWD = 1.9(4). This is compelling evidence that most m/z 134 was incorporated into the metallic aggregates as Ba and not Cs, unlike m/z 133, 135, and 137. The half-life of ^{134}Cs is 2.07 years, comparable to the age depicted in Fig. 7. Therefore, more than half of the ^{134}Cs present at the start of this timescale would have decayed to ^{134}Ba. This correlation further supports the finding that phases within the metallic aggregates preferentially sequestered Ba relative to Cs. The scatter about the regression line may be due in part to fractionation between ^{134}Cs and ^{134}Ba. The presence of ^{134}Ba also indicates that ^{134}Cs was being produced by neutron capture on ^{133}Cs during criticality. The slope of the regression line would typically indicate the neutron fluence, however stable Cs is monoisotopic, making it impossible to deconvolve the primordial and fissionogenic components of ^{133}Cs. If we use ^{138}Ba* as a proxy for ^{133}Cs and adjust the slope by the expected fission yield ratio ^{133}Cs*/^{138}Ba* = 0.06748/0.06557 = 1.029, we calculate a hypothetical neutron fluence to be 3.7(5) × 10^{20} n·cm^{-2}. This slope is 30–50% less than the calculated neutron fluence from ^{100}Ru:^{99}Tc and agrees with the observed Ba/Cs fractionation seen previously. If there were significant primordial Cs present during criticality, this fluence estimate would be an overestimate, however current levels of ^{133}Cs are similar to ^{135,7}Ba*, so this is unlikely.

4.5.3. Rh & Pd

Rhodium is also an appreciable component of the metallic aggregates. Kikuchi et al. (2010) found that its abundance is ~8× lower than Ru, and the two elemental abundances are slightly anti-correlated between different aggregates. The fission yields of ^{99}(Tc + Ru), ^{101}Ru, ^{102}Ru, and ^{104}Ru are collectively 17.6% relative to 3.9% for ^{103}Rh, indicating that the abundance of Rh in the epsilon phase is approximately 2× lower than the fission yield. This agrees with the data in Fig. 9, where the ^{103}Rh$^+$/^{101}Ru$^+$ ratios span a range of 0.19–0.38 compared to the expected fission yield of 0.72 (Rh/Ru RSF ~ 1.3). In general, both the ^{102}Ru/^{101}Ru and ^{104}(Ru + Pd)/^{101}Ru ratios in the aggregates are uniform, with the main variations in ^{104}(Ru + Pd)/^{101}Ru being correlated with the presence of ^{103}Rh. The expected fission yield of ^{104}Ru/^{101}Ru is shown by a dashed horizontal line, which is slightly higher than the minimum of the data. This could indicate that this sample near the center of the reactor core had a slightly lower complement of ^{238}U and/or ^{239}Pu fission than the bulk sample measured by (Hidaka and Holliger, 1998). Without neutron capture to produce ^{104}Pd, the data would be expected to fall along or parallel to this line. The regression line in Fig. 9 fits the data well, with a slope = 0.333(53), intercept = 0.427(11), and MSWD = 1.2(7). The slope of the regression corresponds to the burnup of ^{103}Rh ($\sigma_{c,\ 103Rh} = 133.2 + 1045\cdot r$ barns) to ^{104}Pd and is equivalent to a neutron fluence of 3.3(8) × 10^{20} n·cm^{-2}. This fluence is approximately 27% of the calculated value for the NAUTILUS FOV #1 aggregate, which may be indicative of the incompatibility and loss of Pd from these regions. Generally, the abundance of Pd in the aggregates is ~100× lower than the expected fission yield (see the ^{105}Pd$^+$/^{101}Ru$^+$ ratios in Fig. 2 and Fig. A3), while Pd is relatively more abundant in the uraninite than Ru or Rh (Fig. A4). The ^{104}(Ru + Pd)$^+$/^{105}Pd$^+$ and ^{103}Rh$^+$/^{105}Pd$^+$ ratios from the same locations also show a linear relationship (Fig. A7). However, the excess scatter is very large (MSWD = 65), so this regression is not as useful.

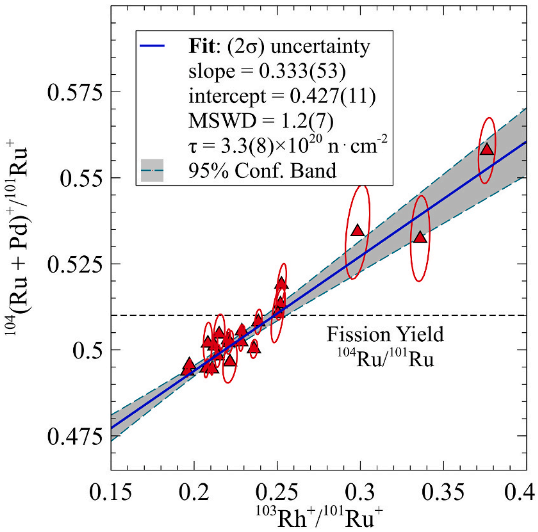

Fig. 9. Correlation between ^{103}Rh/^{101}Ru + and ^{104}(Ru + Pd)/^{101}Ru$^+$ from NAUTILUS FOVs. Ruthemium-102 and 104 are almost perfectly correlated, so excesses in m/z = 104 are expected to be ^{104}Pd from neutron capture on ^{103}Rh. The regression slope yields an estimated neutron fluence of 3.3(8) × 10^{20} n·cm^{-2}, roughly 27% of that calculated from ^{100}Ru vs. ^{99}Ru in NAUTILUS FOV #1. Loss of Pd from the aggregates may explain this deficit.

4.5.4. Pb

In addition to NanoSIMS isotope images of two metallic aggregates, we collected Pb and U isotope image data from nearby uraninite and galena crystals, and Pb, Th, and U isotope spot measurements from uraninite using the NAUTILUS. Fig. 10 shows an inverse Pb–Pb isochron derived from the uraninite and galena data, which intercepts the ^{207}Pb/^{206}Pb axis at 0.0523(10). The ^{207}Pb/^{206}Pb ratios were corrected for the depletion of ^{235}U at each spot; where the ^{235}U/^{238}U ratios ranges from 0.368% to 0.433%. Since galena does not contain U, the ^{235}U/^{238}U ratio from adjacent image regions was used. The fit intercept corresponds to an age of 298 ± 44 Ma (2σ) using $\lambda_{235} = 9.8485 \times 10^{-10}$ yr^{-1}

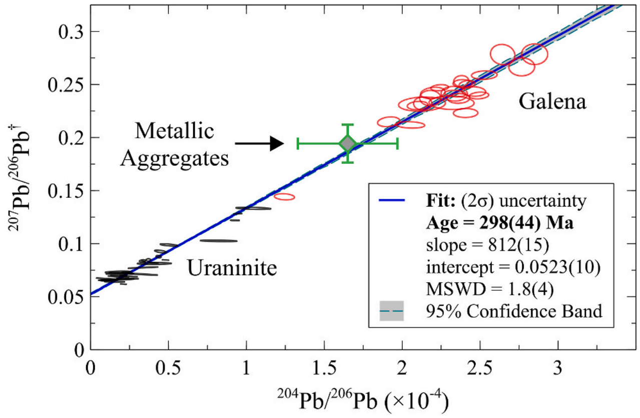

Fig. 10. Inverse Pb–Pb isochron between uraninite and galena data with ^{207}Pb/^{206}Pb corrected for ^{235}U depletion. Intercept at 0.0523(10) corresponds to an age of 298(44) Ma. Inferred ^{204}Pb for aggregates based on analyses from Kikuchi et al. (2010), which was excluded from the regression.

and $\lambda_{238} = 1.55125 \times 10^{-10}$ yr^{-1} (Jaffey et al., 1971; Steiger and Jäger, 1977), and has an MSWD of 1.8(4). The inferred intercept age corresponds to common Pb ratios: $^{206}Pb/^{204}Pb = 18.24$, $^{207}Pb/^{204}Pb = 15.60$, and $^{208}Pb/^{204}Pb = 38.08$ (Stacey and Kramers, 1975). We could not measure ^{204}Pb in the metallic aggregates with the employed NanoSIMS setup. However, Kikuchi et al. (2010) found an average $^{204}Pb/^{206}Pb$ composition of the metallic aggregates to be $1.65 \times 10^{-4} \pm 2.28 \times 10^{-5}$ (1 sd), so we used this value to infer the abundances of ^{204}Pb in our NanoSIMS measurements. Using this approximation, the average composition of the metallic aggregates is shown in Fig. 10 (without accounting for correlated errors), where it appears to fall on a mixing line between the uraninite and galena compositions. This makes sense considering that the metallic aggregates tend to contain appreciable PbS contents, whose magnitude is inversely proportional to the Ru + Rh + Te + As + S abundance in RZ13 (Hidaka et al., 1999; Holliger, 1994; Kikuchi et al., 2010).

4.5.5. *Bi*

We found that the presence of Bi in most of the metallic aggregate area was well correlated with the abundance of Rh. In addition, we observed several “nuggets” of Bi that did not appear to correlate to any other measured element. Neither Bi nor Rh exhibited any correlation to Pb or S. Fig. A8 (left) shows the Rh:Bi correlation along with a best-fit line. We did not have a reliable standard to measure the Rh/Bi RSF, however, Rh^+ is estimated to ionize 5× more readily than Bi^+ from a metallic Si matrix (Wilson, 1995). Therefore, the slope of the regression line after correcting for RSFs should be greater than 1. Stable, stoichiometric Bi–Rh compounds exist as Bi_4Rh and Bi_2Rh, supporting our qualitative finding of a slope >1 (Kainzbauer et al., 2018). The Bi-rich nuggets and regions corresponding to galena do not fall along this correlation line, with the latter being Bi-depleted. These data were clear outliers and were not included. The inset figure shows EPMA data from several different aggregates from Kikuchi et al. (2010), which also show a general correlation between Bi and Rh, but with a lesser slope. We think these data represent an oversampling of galena relative to our analyses given the approximately 30 μm-sized EPMA spot. However, without a good matrix-matched Bi:Rh standard, a true comparison of the different slopes is not possible. The data from Kikuchi et al. (2010) also show that Bi strongly correlated with Pd (not shown). In addition to the SIMS and EPMA data, Bi–Rh & Bi–Pd nanoparticles have been observed in the Oklo RZs using transmission electron microscopy (TEM) (Utsunomiya and Ewing, 2006). Fig. A8 (right) shows that Bi abundances lack any correlation with Pb or S, with the latter being potentially anti-correlated.

5. Discussion

Two of the primary observations in this work regarding the sequestration of Cs and Ba remain difficult to reconcile. The first is that ^{135}Ba* and ^{137}Ba* were incorporated into the metallic aggregates as Cs, despite vastly different half-lives. These two isotopes were found in similar abundances, despite evidence that Ba was preferentially incorporated by a factor of ~2× . This was interpreted by Groopman et al. (2018) to mean that Cs was efficiently flushed out of the reactor during criticality – otherwise nearly all $m/z = 137$ during and after criticality would be ^{137}Ba, yielding the observed Ba/Cs fractionation pattern. This assumption was reasonable given the high solubility of Cs in water, elevated reactor temperature, and the incompatibility of Cs with uraninite. Based on these assumptions, a closure age anchored to the end of criticality (updated in this work) of 2.7 years was calculated. The presence of ^{134}Ba* at approximately 5% the abundance of ^{138}Ba* complicates this interpretation. The abundance of ^{134}Ba* inferred fluence from the ^{134}Ba*:^{138}Ba* correlation indicates that the $^{133}Cs(n,\gamma)^{134}Cs(\beta^-)^{134}Ba$ reactions were occurring throughout reactor operation. Several thousand years would be required to produce $^{134}(Cs + Ba)^*/^{138}Ba^*$ ratios up to 1% starting from an absence of ^{133}Cs* and ^{138}Ba* (using the average reactor flux), over which time >99% ^{137}Cs* would have decayed to Ba. Likewise, a reservoir that trapped ^{134}Ba until the end of criticality would also have held ^{137}Ba. Therefore, the 2.7 year “age” interpreted from Fig. 7 may instead reflect the characteristic time for flushing Cs and Ba out of the reactor following their production.

One of the metallic aggregates identified by Groopman et al. (2018) was found to be completely encapsulated within a uraninite grain. All other aggregates have been found in cracks between uraninites. This particular aggregate contained an elevated abundance of ^{138}Ba* compared to the others, but no detectable ^{134}Ba*. Unfortunately, definitive statements cannot be made based upon a single outlier. However, we can speculate that most neutron capture on ^{133}Cs did not occur within the time required to exclude Cs from the uraninite. Instead it seems likely that neutron capture on ^{133}Cs occurred while Cs was dissolved in the H_2O moderator or held in secondary minerals, but before being flushed from the reactor. Some neutron capture could have occurred after ^{133}Cs was incorporated into the metallic aggregates, though this would not sufficiently explain the strong correlation between ^{134}Ba* and ^{138}Ba*.

This work highlights several key differences between natural and anthropogenic nuclear fuel, the former in a geologically open setting. Corrosion experiments on the ε-phase from anthropogenic reactor fuel found that Tc leached from the metallic aggregates significantly faster than Ru, Rh, and Pd under oxidizing and reducing conditions (Cui et al., 2004; Utsunomiya and Ewing, 2006). We did not find evidence of significant Tc leaching from the ε-phase. At minimum, any leaching processes that would have affected Tc did not occur until most Tc decayed to Ru, well after criticality. However, we observed that Pd was potentially affected. The lower fluence estimated from the reaction $^{103}Rh(n,\beta^-)^{104}Pd$ could have been the result of Pd loss. In the Oklo fuel, Pd shows a similar affinity for the uraninite and ε-phase, whereas Ru, Rh, and Tc are much more concentrated in the metallic aggregates. An alternative explanation might be that the sequestration of Rh into the aggregates was delayed by approximately half the criticality duration. This would result in the relative depletion of Rh within the aggregates and the “missing” fluence, both of which are low by approximately the same magnitude. However, this is speculative as a mechanism yielding this effect remains unknown.

The Pb mobilization event that we identified (298 ± 22 Ma, 1σ) occurred well after the dolerite dike intrusion (~860 Ma) and the more recent event identified by Evins et al. (2005) at ~500 Ma from RZ16 and Bangombé. Nagy et al. (1991), Gancarz (1978), and Fayek et al. (2002) also identified a similar Pb-loss episode at Oklo occurring 330 ± 150 Ma, 375 ± 25 Ma, and 375 ± 53 Ma, respectively, as the lower intercept of conventional concordia diagrams. Unfortunately, 300 Ma rocks are not present in Gabon, so the cause of this disturbance remains unknown.

The RZs contained low abundances of primordial Bi, so the major source of Bi would have been through the production of long-lived ^{237}Np ($t_{1/2} = 2.1$ Ma), which decayed to ^{209}Bi via ^{233}U ($t_{1/2} = 0.16$ Ma) (Hidaka and Holliger, 1998). There are three reaction pathways to produce ^{237}Np, however a simple 1D neutron-capture/decay model shows that ~94% of the ^{237}Np would have been produced through the α-decay of ^{241}Am ($t_{1/2} = 432.6$ y) via $^{238}U(n,\gamma 2\beta^-)^{239}Pu(n,\gamma)^{240}Pu(n,\gamma)^{241}Pu(\beta^-)^{241}Am(\alpha)^{237}Np$. Most of the remaining 6% would have been produced by neutron capture on ^{236}U ($t_{1/2} = 23.4$ Ma) via $^{235}U(n,\gamma)^{236}U(n,\gamma\beta^-)^{237}Np$. The $^{238}U(n, 2n\beta^-)^{237}Np$ reaction requires fast neutrons above 6 MeV, and the cross section is small. Essentially all ^{237}Np produced in RZ13 would be live at the end of criticality. Discounting migration and shielding effects, the expected concentration of ^{237}Np in the reactor at the end of criticality would be almost 0.2%. The primary question is whether the current correlation of Rh and Bi reflects the final distribution of ^{237}Np or a redistribution of ^{209}Bi millions of years after decay.

Lead was redistributed within the RZs, notably due to the intrusion of a dolerite dike 860 Ma ago and as recently as 300 Ma. Hidaka and Holliger (1998) have suggested that Bi was not redistributed in the RZs because the rocks peripheral to the reactor core were not enriched in Bi as they were in Pb. Bismuth abundances lack any correlation with Pb or S, with the latter being potentially anti-correlated. This is despite Bi and Pb being able to form a eutectic at low temperatures (123.5 °C), and Bi commonly forming sulfide and plumbous sulfide compounds in ores. Neptunium is known to form metallic compounds with Rh, Pd, and Ru under reducing conditions (Erdmann and Keller, 1973; National Research Council, 1974). However, the binary compounds tend to be of the form NpM_3 (M = Pd,Rh) or NpM_2 (M = Ru), unlike the stable Bi–Rh compounds (Erdmann and Keller, 1973; Yoshida et al., 2011), indicating that some substitution would have occurred if the Bi in the Rh and Pd alloys were originally Np. The evidence for Np incorporation into the metallic aggregates as Rh- and Pd-alloys remains circumstantial. However, this scenario is a reasonable possibility in our judgement, based upon: 1) the correlation of Bi with Rh and Pd from SIMS and EPMA, and the presence of binary alloys in TEM analyses; 2) the lack of evidence for Bi redistribution, unlike Pb; and 3) the lack of Bi–Pb and Bi-(Pb)–S minerals, which might be expected if the Bi–Rh and Bi–Pd alloys did not evolve from Np–Rh and Np–Pd.

6. Conclusions

Amidst the field of incredible natural nuclear reactor sites in present-day Gabon, RZ13 was singular. RZ13 operated over a shorter time and with a higher neutron flux and harder spectrum than its neighbors, yielding the most depleted natural uranium on Earth and a large inventory of fission products. The ε-phase metallic aggregates at RZ13 are much larger than those in RZ10 and from anthropogenic reactors, which has allowed us to investigate their affinities for volatile, noble metal, and transition metal fission products on the nano-to-micrometer scale. Secondary aluminous hydroxy phosphate minerals in RZ13 that formed during criticality exhibit large Cs and Ba abundances, but these are of terrestrial isotopic composition, likely reflecting exchange after criticality (Dymkov et al., 1997; Groopman et al., 2018). This contrasts to the large abundances of sequestered noble gases, such as Xe, in the aluminous phosphates, which retain their fissionogenic signatures (Meshik et al., 2000, 2004). Isotopic equilibration of Cs and Ba is apparent throughout the rest of the reactor sites, but does not appear to have strongly influenced the ε-phase. Two important isotopes for short- and medium-term nuclear waste storage, ^{99}Tc and ^{137}Cs, were found to be preferentially sequestered within the aggregates. Some phases within the metallic aggregates captured Tc in abundances 5× greater Ru, the most abundant noble metal. Fissionogenic Tc and Cs were found in their highest abundances in separate phases. The radioactive isotopes of Tc and Cs have long since decayed to Ru and Ba, respectively, however stable ^{133}Cs was found to have been retained in the aggregates in its original abundance, comparable to other Cs and Ba fission products. This is despite the volatility and solubility of Cs, and the geological perturbations over the intervening 2 Ga. Therefore, we have found evidence of effective radioactive Cs sequestration across four different timescales: spanning the half-lives of ^{134}Cs ($t_{1/2}$ = 2.1 y), ^{137}Cs ($t_{1/2}$ = 30 y), ^{135}Cs ($t_{1/2}$ = 2.3 Ma), and ^{133}Cs (stable).

Based upon the relative proportions of $^{135}Ba^*/^{138}Ba^*$ and $^{137}Ba^*/^{138}Ba^*$, we determined a closure age for Cs of 2.7 ± 0.6 years (2σ). Groopman et al. (2018) interpreted this closure age to be anchored to the termination of reactor criticality given the large disparity in the half-lives of ^{137}Cs and ^{135}Cs, which would otherwise yield discernible Cs/Ba fractionation. This fractionation is visible from the $^{135}Ba^*/^{138}Ba^*$ and $^{137}Ba^*/^{138}Ba^*$ ratios, which are mostly less than 1, despite these isotopes having similar fission yields. However, the large abundances of ^{134}Ba* (from neutron capture on ^{133}Cs) and its correlation with ^{138}Ba* indicate that ^{133}Cs*, ^{134}Cs* and/or ^{134}Ba* were being sequestered actively during criticality. This suggests that the 2.7 year "age" calculated here reflects the characteristic time to flush fissionogenic Cs and Ba out of the reactor following their production. This would allow for a slow accumulation of correlated ^{134}Ba* and ^{138}Ba* without inducing significant fractionation between ^{135}Ba* and ^{137}Ba*.

The inferred neutron fluence from the correlation of ^{100}Ru and ^{99}Ru, (7.6–12.1) × 10^{20} n·cm^{-2}, agreed with previous estimates for RZ13, indicating that the metallic aggregates began to form early and that Ru and Tc were retained well within the reactor. Isotopes of Pd and Rh yield a lower fluence estimate, which indicates that fractionation or leaching of Pd from the aggregates may have occurred. Overall, the aggregates contain abundances of Pd and Rh that are lower than their fission yields relative to Ru. Leeching experiments have demonstrated that Mo in the ε-phase particles would be the most sensitive to removal under both reducing and oxidizing conditions (Cui et al., 2004). This agrees with work which found that Mo was mostly removed from the aggregates (Utsunomiya and Ewing, 2006). According to Cui et al. (2004), Tc would be expected to be the next most sensitive element to leeching, with Ru, Rh, and Pd being less sensitive. We found that Tc was well retained in most aggregate phases, whereas Pd may have been more susceptible to loss in the geological setting of RZ13.

RZ13 likely produced more ^{237}Np than other reactor sites, predominantly through successive neutron captures on ^{238}U and α-decay of ^{241}Am. Eventually, ^{237}Np decayed to ^{209}Bi. Within the metallic aggregates, Bi was found to correlate with Rh and Pd, and had no discernible relationship to Pb or S. This is despite the widespread redistribution of Pb in the reactors and the recrystallization of galena, but no apparent Bi–S or Bi–Pb phases. The Oklo RZs have low primordial Bi contents, and Bi was not previously observed to have been lost from the reactor (Hidaka and Holliger, 1998). We therefore speculate that the Bi–Rh and Bi–Pd alloys found in the Oklo RZs (Utsunomiya and Ewing, 2006) could have been the result of primary Np–Rh and Np–Pd formation during or shortly after criticality.

Lead-lead data from the RZ13 uraninite and galenas adjacent to the metallic aggregates indicated a Pb-loss or closure age of 298 ± 44 Ma (2σ). Redistribution of Pb has been widely observed in the RZs, most notably due to the intrusion of a dolerite dyke ~860 Ma ago and potentially by fluid interactions during the Pan-African orogeny at ~500 Ma (Evins et al., 2005). The uncertainty on the age estimate is tight enough to clearly distinguish it from other earlier events, even it is too broad to specifically point to a single event. In any case, 300 Ma old rocks are not present in Gabon for potential verification.

The study of the Oklo natural nuclear reactors continues to yield important information regarding the interaction of SNF with the environment over the long term. Notably, they have also revealed clues regarding the complex fractionation and sequestration of fission products that are relevant on generational timescales, despite their operation 2 Ga ago. This work represents the first coordinated application of the NAUTILUS and NanoSIMS mass spectrometers to the study of fission and burnup product behavior in the SNF. The NAUTILUS mitigates the complex and omnipresent molecular background in SIMS analyses of heterogeneous samples, particularly SNF, which contains constituents from much of the periodic table. The NanoSIMS has allowed for the first time the nano-scale interrogation of fission product sequestration in the ε-phase. These techniques have allowed for a visual and quantitative assessment of the behavior of fissionogenic Tc and Cs (among others), which is important for improving the safety of nuclear reactors and spent fuel storage.

Declaration of competing interest

The authors declare that they have no known competing financial interests or personal relationships that could have appeared to influence the work reported in this paper.

Acknowledgements

This work was funded by the Office of Naval Research through the NRL Base program. We thank Maurice Pagel and François Gauthier-Lafaye for the Oklo sample; Philippe Holliger for sharing copies of his

1991 and 1994 reports; Hiroshi Hidaka for discussions. We appreciate the thoughtful reviews that improved the paper.

Appendix A.1

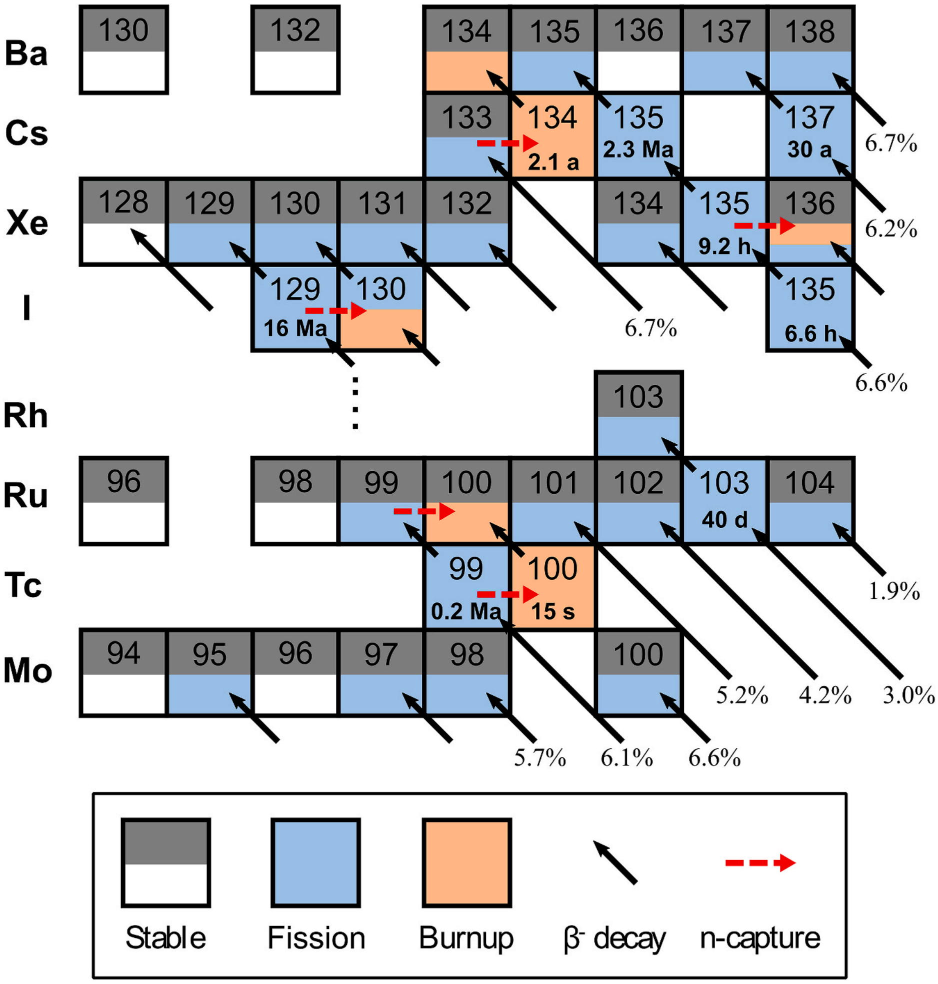

Fig. A1. Excerpted chart of the nuclides for Mo, Tc, Ru, and Rh; I, Xe, Cs, and Ba. Fission products, beta decay pathways, and neutron capture reactions are shown. Isotopes with short half-lives have generally been omitted. Fission yields given in % are from a 74.9% ^{235}U, 17.9% ^{238}U, and 7.2% ^{239}Pu mixture of thermal & epithermal fission.

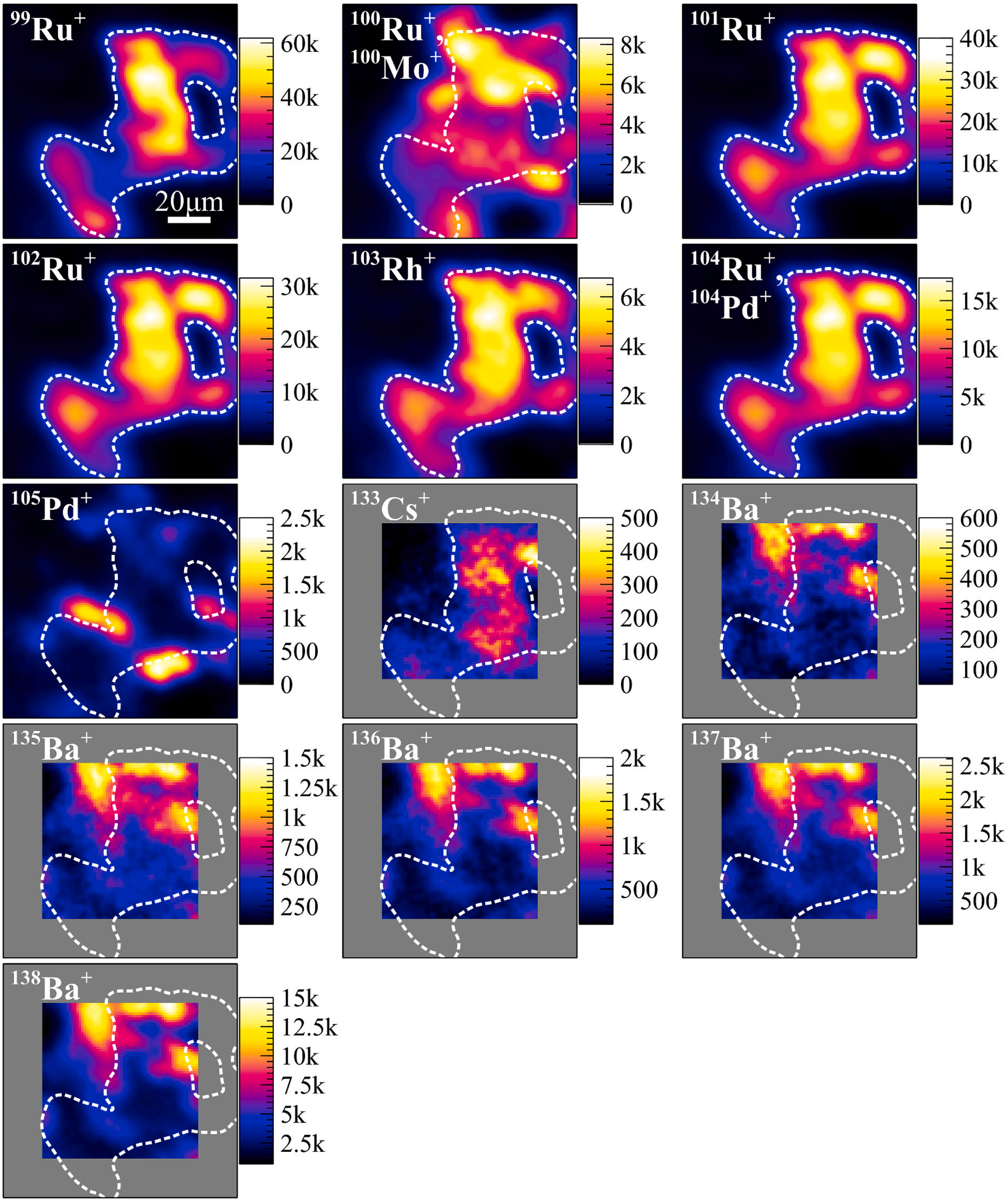

Fig. A2. Isotope images from NAUTILUS FOV #2. This FOV contains a larger abundance of Mo, which interferes with Ru at m/z = 100. Cesium and barium data were collected over a smaller FOV, which was padded by a grey frame in these images.

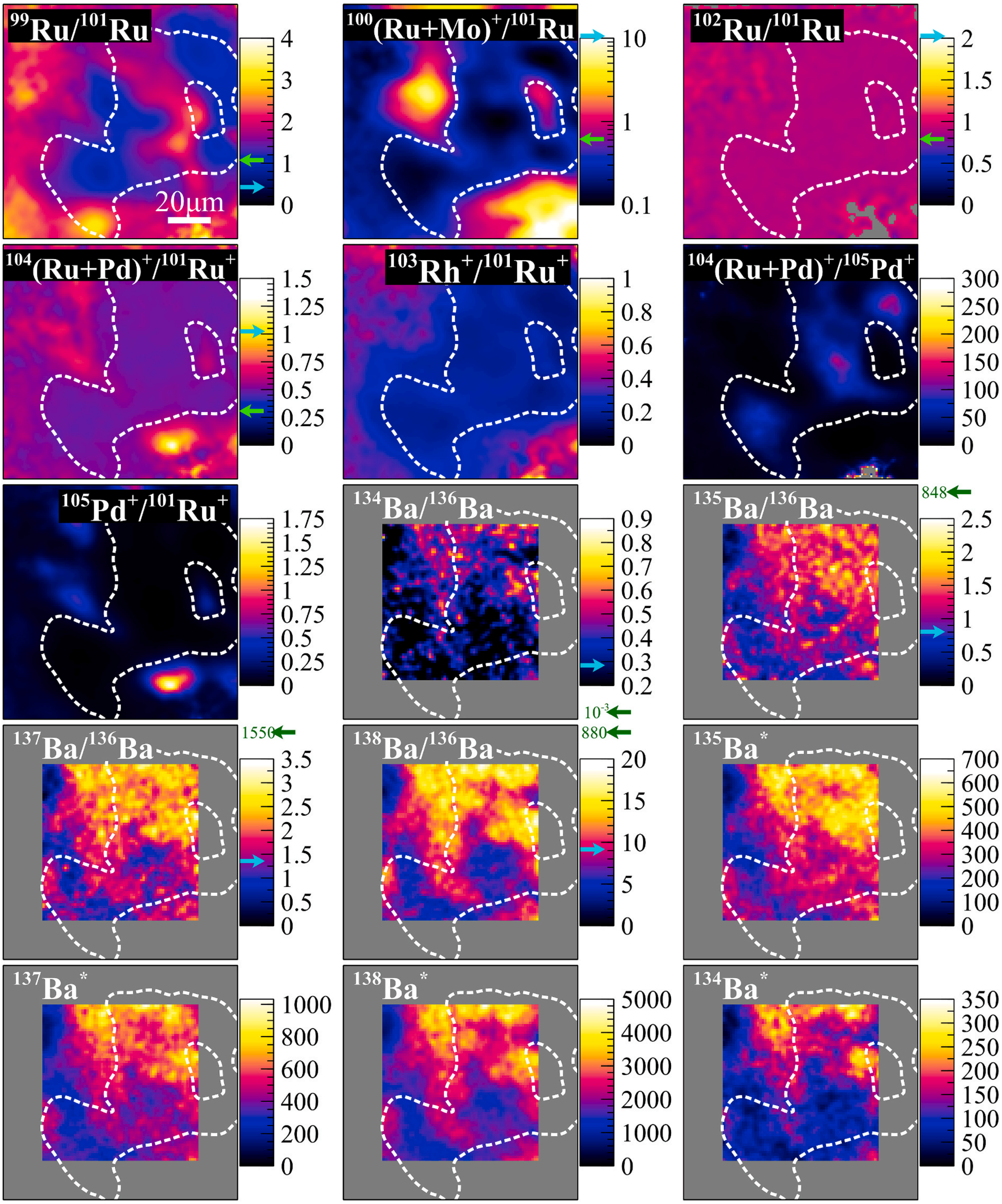

Fig. A3. Isotope ratio images from NAUTILUS FOV #2. The enhancements in Ba* extend beyond the aggregate outline.

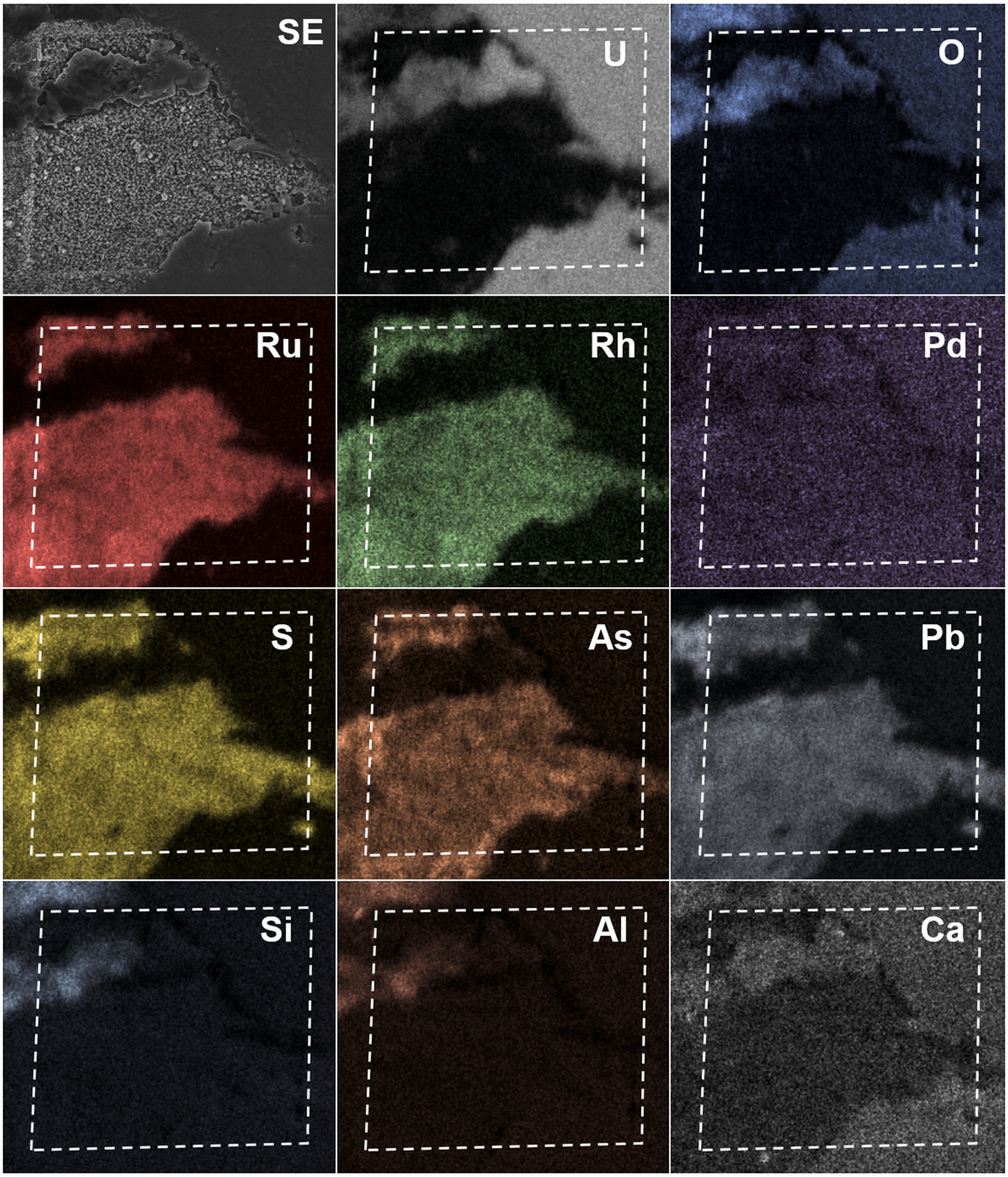

Fig. A4. Qualitative EDXS maps collected post-NanoSIMS from FOV #1. EDXS intensities have been rescaled for visual clarity and smoothed across a 2 pixel-wide kernel. The white, dashed outline indicates the extent of the NanoSIMS analysis, particularly visible in the secondary electron (SE) image.

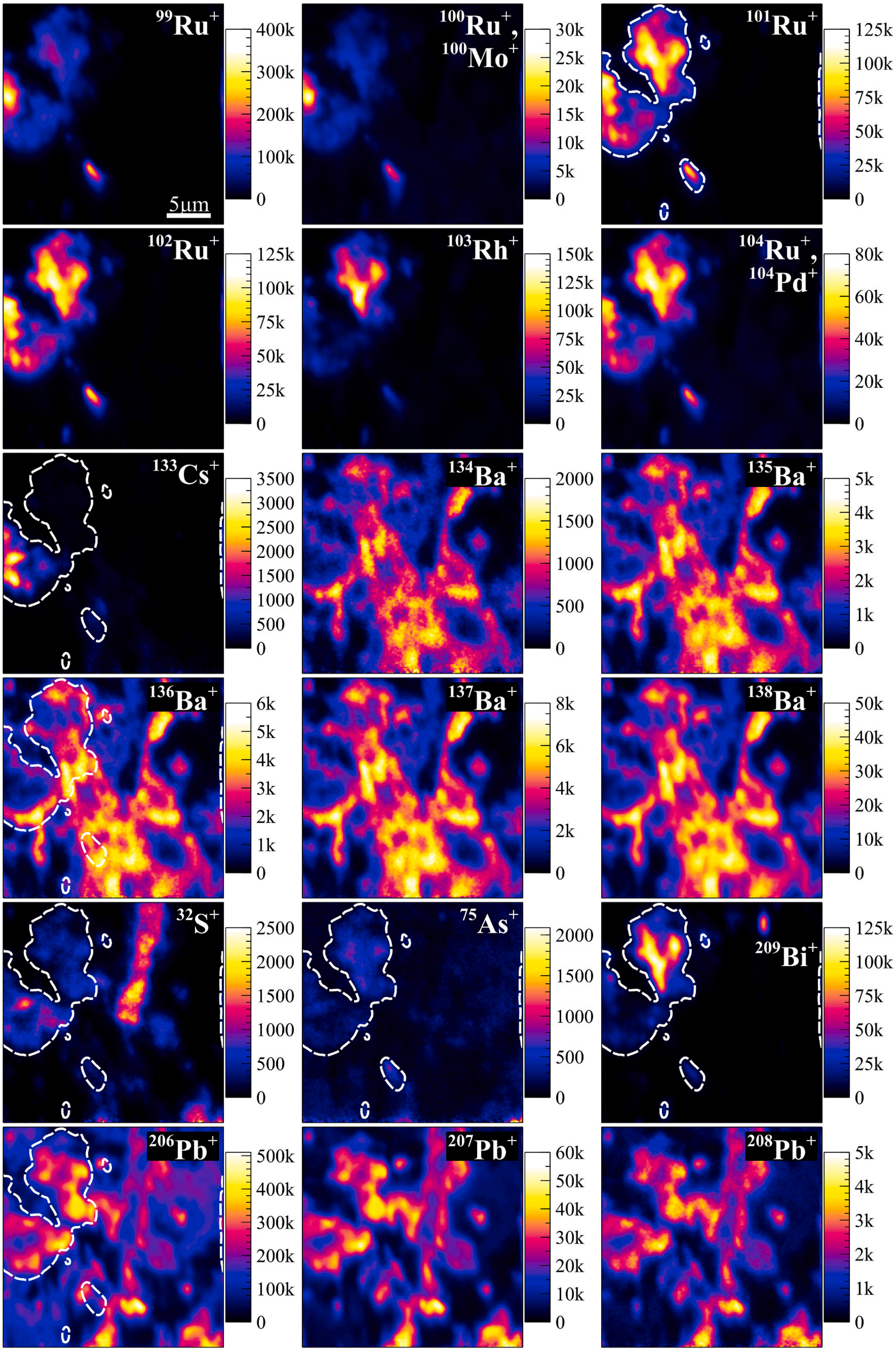

Fig. A5. Isotope images from NanoSIMS FOV #2.

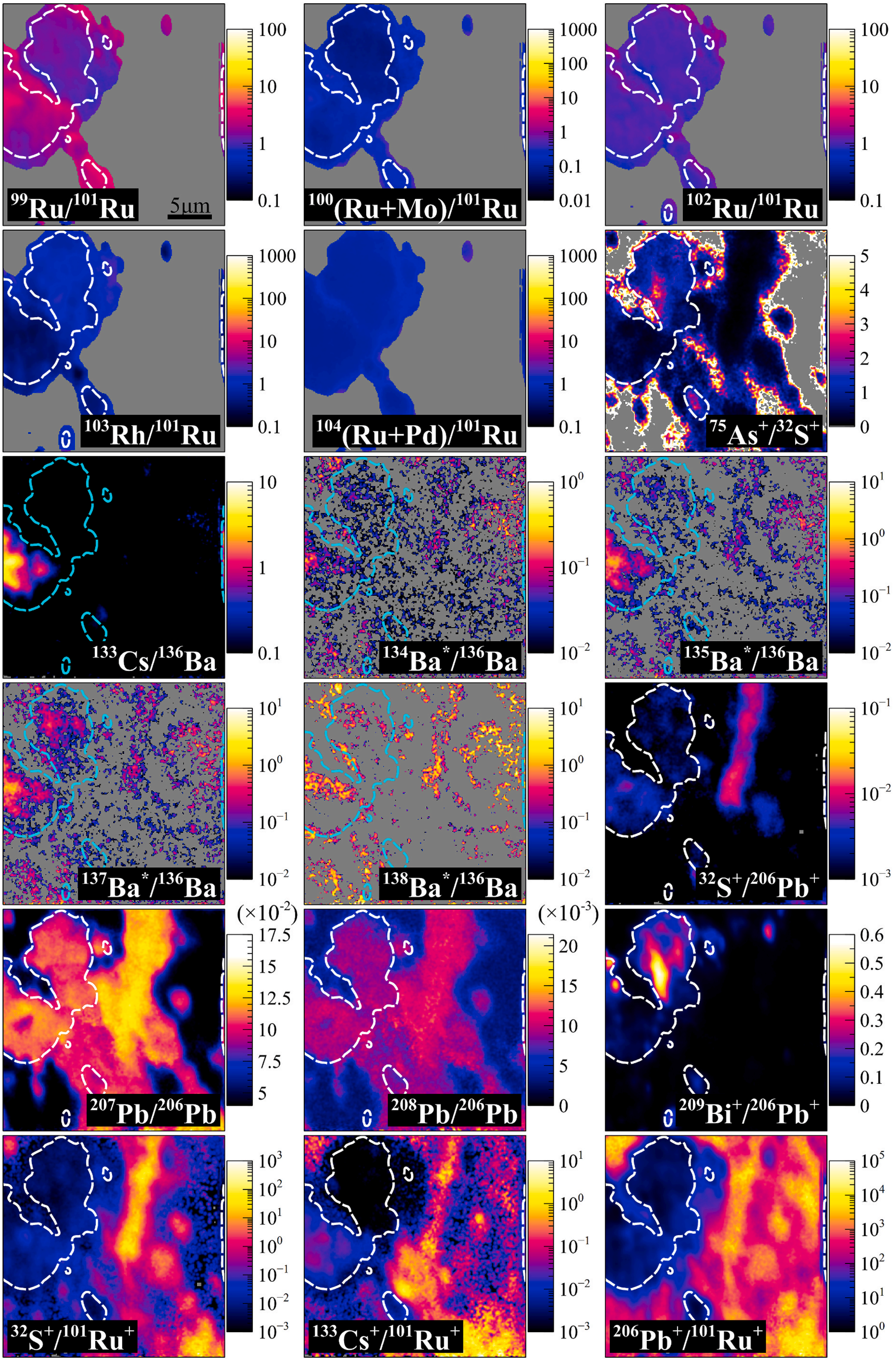
^{99}Ru/^{101}Ru
5μm
100
10
1
0.1
^{100}(Ru+Mo)/^{101}Ru
1000
100
10
1
0.1
0.01
^{102}Ru/^{101}Ru
100
10
1
0.1
^{103}Rh/^{101}Ru
1000
100
10
1
0.1
^{104}(Ru+Pd)/^{101}Ru
1000
100
10
1
0.1
^{75}As^{+}/^{32}S^{+}
5
4
3
2
1
0
^{133}Cs/^{136}Ba
10
1
0.1
^{134}Ba*/^{136}Ba
10^{0}
10^{-1}
10^{-2}
^{135}Ba*/^{136}Ba
10^{1}
10^{0}
10^{-1}
10^{-2}
^{137}Ba*/^{136}Ba
10^{1}
10^{0}
10^{-1}
10^{-2}
^{138}Ba*/^{136}Ba
10^{1}
10^{0}
10^{-1}
10^{-2}
^{32}S^{+}/^{206}Pb^{+}
10^{-1}
10^{-2}
10^{-3}
^{207}Pb/^{206}Pb
($\times 10^{-2}$)
17.5
15
12.5
10
7.5
5
^{208}Pb/^{206}Pb
($\times 10^{-3}$)
20
15
10
5
0
^{209}Bi^{+}/^{206}Pb^{+}
0.6
0.5
0.4
0.3
0.2
0.1
0
^{32}S^{+}/^{101}Ru^{+}
10^{3}
10^{2}
10^{1}
10^{0}
10^{-1}
10^{-2}
10^{-3}
^{133}Cs^{+}/^{101}Ru^{+}
10^{1}
10^{0}
10^{-1}
10^{-2}
10^{-3}
^{206}Pb^{+}/^{101}Ru^{+}
10^{5}
10^{4}
10^{3}
10^{2}
10^{1}
10^{0}

Fig. A6. Isotope ratio images from NanoSIMS FOV #2.

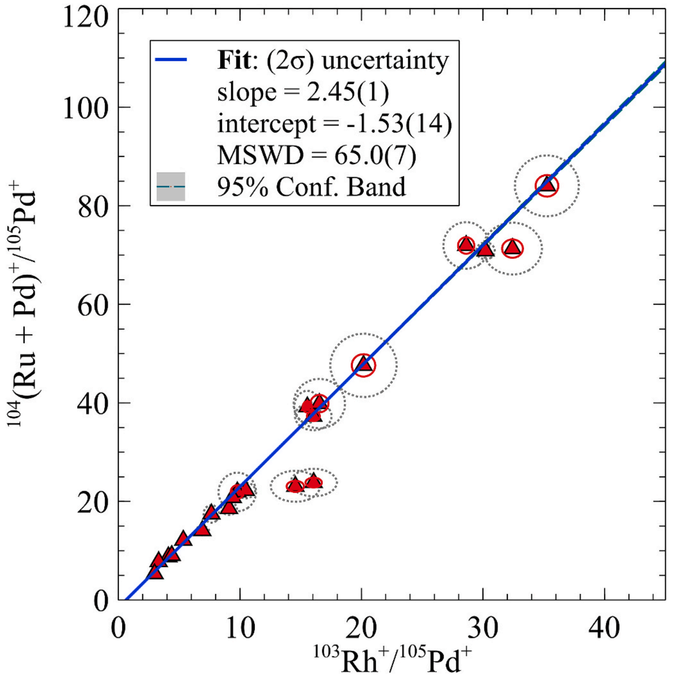

Fig. A7. Linear correlation between $^{104}(Ru + Pd)^+/^{105}Pd^+$ and $^{103}Rh^+/^{105}Pd^+$ from NAUTILUS data. The counting statistical uncertainties on the data points underestimate the variation about the regression. Estimated uncertainties are shown on the data (dashed ellipses) that would reduce the MSWD to 1 (scaling all uncertainties equally).

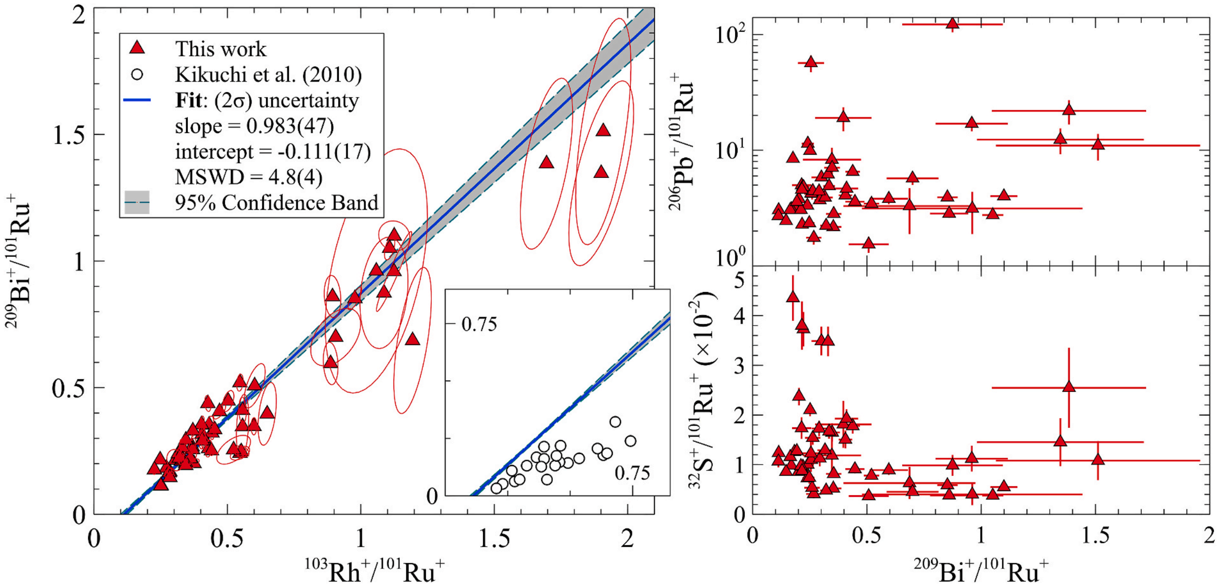

Fig. A8. Correlation between ^{103}Rh and ^{209}Bi, excluding Bi-only nuggets and galena inclusions. This correlation hints at the potential formation of Np:Rh compounds. EPMA data from Kikuchi et al. (2010) shown in the inset for comparison. We did not have an appropriate Bi:Rh:Ru standard, so the slopes and extents of the data are only qualitative. Bismuth is not correlated with either Pb or S.

Appendix B. Supplementary data

Supplementary data to this article can be found online at https://doi.org/10.1016/j.apgeochem.2021.105047.

References

Adriaens, A., Adams, F., 1991. Comparison between the precision characteristics of the magnetic and electrostatic peak switching systems in secondary ion mass-spectrometry. Int. J. Mass Spectrom. Ion Process. 108, 41–52.

Beers, T.C., Flynn, K., Gebhardt, K., 1990. Measures of location and scale for velocities in clusters of galaxies - a robust approach. Astronomical J. 100.

Bodu, R., Bouzigues, H., Morin, N., Pfiffelmann, J.P., 1972. Sur l'existence d'anomalies isotopiques recontrees dans l'uranium du Gabon. C. R. Acad. Sci. Paris 275, 1731.

Bonhomme, M., Leclerc, J., Weber, F., 1978. Etude radiochronologique complémentaire de la série du Francevillien et de son environnement. Natural Fission Reactors 19–23.

Bonhomme, M.G., Gauthier-Lafaye, F., Weber, F., 1982. An example of lower proterozoic sediments: the Francevillian in Gabon. Precambrian Res. 18, 87–102.

Brookins, D.G., Lee, M.J., Mukhopadhyay, B., Bolivar, S.L., 1975. Search for fission-produced Rb, Sr, Cs and Ba at Oklo. IAEA, Vienna.

Christl, M., Vockenhuber, C., Kubik, P.W., Wacker, L., Lachner, J., Alfimov, V., Synal, H. A., 2013. The ETH zurich AMS facilities: performance parameters and reference materials. Nuclear instruments and methods in physics research section B. Beam Interactions with Materials and Atoms 294, 29–38.

Cui, D., Low, J., Sjöstedt, C.J., Spahiu, K., 2004. On Mo-Ru-Tc-Pd-Rh-Te alloy particles extracted from spent fuel and their leaching behavior under Ar and H2 atmospheres. Radiochimica Acta 92.

Curtis, D., Benjamin, T., Gancarz, A., Loss, R., Rosman, K., DeLaeter, J., Delmore, J.E., Maeck, W.J., 1989. Fission product retention in the Oklo natural fission reactors. Appl. Geochem. 4, 49–62.

De Laeter, J.R., Hidaka, H., 2007. The role of mass spectrometry to study the Oklo-Bangombe natural reactors. Mass Spectrom. Rev. 26, 683–712.

Dymkov, Y., Holliger, P., Pagel, M., Gorshkov, A., Artyukhina, A., 1997. Characterization of a La-Ce-Sr-Ca aluminous hydroxy phosphate in nuclear zone 13 in the Oklo uranium deposit (Gabon). Miner. Deposita 32, 617–620.

Efron, B., Tibshirani, R., 1986. Bootstrap methods for standard errors, confidence intervals, and other measures of statistical accuracy. Stat. Sci. 1, 54–75.

Erdmann, B., Keller, C., 1973. Actinide(lanthanide)-noble metal alloy phases, preparation and properties. J. Solid State Chem. 7, 40–48.

Evins, L.Z., Jensen, K.A., Ewing, R.C., 2005. Uraninite recrystallization and Pb loss in the Oklo and Bangombé natural fission reactors. Gabon. Geochimica et Cosmochimica Acta 69, 1589–1606.

Fayek, M., Jensen, K.A., Ewing, R.C., Riciputi, L.R., 2002. In situ isotopic analysis of uraninite microstructures from the oklo-okélobondo natural fission reactors, Gabon. MRS Online Proceedings Library Archive 713.

Freeman, S.P.H.T., Ramsey, C.B., Hedges, R.E.M., 1994. Imaging AMS. Nuclear Instruments and Methods in Physics Research Section B. Beam Interactions with Materials and Atoms 92, 231–236.

Gancarz, A.J., 1978. U-Pb age (205x109 years) of the Oklo uranium deposit. IAEA, international atomic energy agency (IAEA).

Gauthier-Lafaye, F., Holliger, P., Blanc, P.L., 1996. Natural fission reactors in the Franceville basin, Gabon: a review of the conditions and results of a "critical event" in a geologic system. Geochem. Cosmochim. Acta 60, 4831–4852.

Groopman, E.E., Grabowski, K.S., Fahey, A.J., Koop, L., 2017. Rapid, molecule-free, in situ rare earth element abundances by SIMS-SSAMS. J. Anal. Atomic Spectrom. 32, 2153–2163.

Groopman, E.E., Willingham, D.G., Fahey, A.J., Grabowski, K.S., 2020. An overview of NRL's NAUTILUS: a combination SIMS-AMS for spatially resolved trace isotope analysis. J. Anal. Atomic Spectrom. 35, 600–625.

Groopman, E.E., Willingham, D.G., Meshik, A.P., Pravdivtseva, O.V., 2018. Discovery of fissionogenic Cs and Ba capture five years after Oklo reactor shutdown. Proc. Natl. Acad. Sci. U. S. A. 115, 8676–8681.

Hidaka, H., 2020. In: A Review of in Situ Isotopic Studies of the Oklo and Bangombé Natural Fission Reactors Using Microbeam Analytical Techniques. Minerals 10.

Hidaka, H., Gauthier-Lafaye, F., 2008. Ba isotopic signature for early differentiation between Cs and Ba in natural fission reactors. Geochem. Cosmochim. Acta 72, 4123–4135.

Hidaka, H., Holliger, P., 1998. Geochemical and neutronic characteristics of the natural fossil fission reactors at Oklo and Bangombé. Gabon. Geochimica et Cosmochimica Acta 62, 89–108.

Hidaka, H., Holliger, P., Gauthier-Lafaye, F., 1999. Tc/Ru fractionation in the Oklo and Bangombé natural fission reactors. Gabon. Chem. Geol. 155, 323–333.

Hidaka, H., Holliger, P., Masuda, A., 1993a. Evidence of fissiogenic Cs estimated from Ba isotopic deviations in an Oklo natural reactor zone. Earth Planet Sci. Lett. 114, 391–396.

Hidaka, H., Konishi, T., Masuda, A., 1992. Reconstruction of cumulative fission yield curve and geochemical behaviors of fissiogenic nuclides in the Oklo natural reactors. Geochem. J. 26, 227–239.

Hidaka, H., Shinotsuka, K., Holliger, P., 1993b. Geochemical behaviour of 99Tc in the Oklo natural fission reactors. Radiochimica acta 63.

Holliger, P., 1991. Les nouvelles zones de reaction d'Oklo: datation U-Pb et caracterisation in-situ des produits de fission a l'analyseur ionique, Oklo - analogues Naturels, CEN Grenoble.

Holliger, P., 1994. Terme Source: caracterisation Isotopique, Parametres Nucleaires et Modelisation, Programme Oklo - analogues Naturels. Commissariat a L'energie Atomique, CEN Cadarache. CCE n° F112W-CT91-0071.

Jaffey, A.H., Flynn, K.F., Glendenin, L.E., Bentley, W.C., Essling, A.M., 1971. Precision measurement of half-lives and specific activities of U235 and U238. Phys. Rev. C 4, 1889–1906.

Kainzbauer, P., Richter, K.W., Ipser, H., 2018. The binary Bi-Rh phase diagram: stable and metastable phases. J. Phase Equilibria Diffus. 39, 17–34.

Kikuchi, M., Hidaka, H., Gauthier-Lafaye, F., 2010. Formation and geochemical significance of micrometallic aggregates including fissiogenic platinum group elements in the Oklo natural reactor. Gabon. Geochimica et Cosmochimica Acta 74, 4709–4722.

Loss, R.D., De Laeter, J.R., Rosman, K.J.R., Benjamin, T.M., Curtis, D.B., Gancarz, A.J., Delmore, J.E., Maeck, W.J., 1988. The Oklo natural reactors: cumulative fission yields and nuclear characteristics of Reactor Zone 9. Earth Planet Sci. Lett. 89, 193–206.

Mao, P.H., Burnett, D.S., Coath, C.D., Jarzebinski, G., Kunihiro, T., McKeegan, K.D., 2008. MegaSIMS: a SIMS/AMS hybrid for measurement of the Sun's oxygen isotopic composition. Appl. Surf. Sci. 255, 1461–1464.

Meshik, A.P., Hohenberg, C.M., Pravdivtseva, O.V., 2004. Record of cycling operation of the natural nuclear reactor in the Oklo/Okelobondo area in Gabon. Phys. Rev. Lett. 93, 182302.

Meshik, A.P., Kehm, K., Hohenberg, C.M., 2000. Anomalous xenon in zone 13 Okelobondo. Geochem. Cosmochim. Acta 64, 1651–1661.

Nagy, B., Gauthier-Lafaye, F., Holliger, P., Davis, D.W., Mossman, D.J., Leventhal, J.S., Rigali, M.J., Parnell, J., 1991. Organic matter and containment of uranium and fissiogenic isotopes at the Oklo natural reactors. Nature 354, 472–475.

National Research Council, 1974. Radiochemistry of Neptunium. The National Academies Press, Washington, DC.

Naudet, R., Horowitz, J., 1991. Oklo: des réacteurs nucléaires fossiles : étude physique. In: Eyrolles : Commissariat à l'Energie Atomique (Paris).

Ogliore, R.C., Huss, G.R., Nagashima, K., 2011. Ratio estimation in SIMS analysis. Nucl. Instrum. Methods Phys. Res. Sect. B Beam Interact. Mater. Atoms 269, 1910–1918.

Ruffenach, J.C., Menes, J., Devillers, C., Lucas, M., Hagemann, R., 1976. Etudes chimiques et isotopiques de l'uranium, du plomb et de plusieurs produits de fission dans un echantillon de minerai du reacteur naturel d'Oklo. Earth Planet Sci. Lett. 30, 94–108.

Savary, V., Pagel, M., 1997. The effects of water radiolysis on local redox conditions in the Oklo, Gabon, natural fission reactors 10 and 16. Geochem. Cosmochim. Acta 61, 4479–4494.

Slodzian, G., Lorin, J.C., Dennebouy, R., Havette, A., 1984. Isotopic measurements at high mass resolution by electrostatic peak switching. In: Benninghoven, A., Okano, J., Shimizu, R., Werner, H.W. (Eds.), Secondary Ion Mass Spectrometry SIMS IV. Springer, Berlin.

Stacey, J.S., Kramers, J.D., 1975. Approximation of terrestrial lead isotope evolution by a two-stage model. Earth Planet Sci. Lett. 26, 207–221.

Steiger, R.H., Jäger, E., 1977. Subcommission on geochronology: convention on the use of decay constants in geo- and cosmochronology. Earth Planet Sci. Lett. 36, 359–362.

Utsunomiya, S., Ewing, R.C., 2006. The fate of the epsilon phase (Mo-Ru-Pd-Tc-Rh) in the UO2 of the Oklo natural fission reactors. Radiochimica Acta 94.

Weber, F., 1968. Une série précambrienne du Gabon: le Francevillien. Sédimentologie, géochimie, relations avec les gîtes minéraux associés. Persée-Portail des revues scientifiques en SHS 28.

Weber, F., Gauthier-Lafaye, F., Whitechurch, H., Ulrich, M., El Albani, A., 2016. The 2-Ga Eburnean Orogeny in Gabon and the opening of the Francevillian intracratonic basins: a review. Compt. Rendus Geosci. 348, 572–586.

Wendt, I., Carl, C., 1991. The statistical distribution of the mean squared weighted deviation. Chem. Geol. Isotope Geosci. Section 86, 275–285.

Wilson, R.G., 1995. SIMS quantification in Si, GaAs, and diamond - an update. Int. J. Mass Spectrom. Ion Process. 143, 43–49.

York, D., Evensen, N.M., Martínez, M.L., De Basabe Delgado, J., 2004. Unified equations for the slope, intercept, and standard errors of the best straight line. Am. J. Phys. 72, 367–375.

Yoshida, Z., Johnson, S.G., Kimura, T., Krsul, J.R., 2011. Neptunium. In: Morss, L.R., Edelstein, N.M., Fuger, J. (Eds.), The Chemistry of the Actinide and Transactinide Elements. Springer Netherlands, Dordrecht, pp. 699–812.